Neutron wavelength estimation on crystal monochromator beamlines.

Anton Eklind Schultz

6th March 2014

Abstract

The world wide shortage of helium-3 is forcing the development of new detectors for neutron spectroscopy. A candidate for new detector design that consists of multiple detection volumes in depth, in contrast to the traditional single volume helium-3 detector, is being developed at ESS in Lund. One advantage of the new design is the possibility of utilising the additional depth dimension to extract information about the beams used in neutron spectroscopy, more exactly their wavelength compositions.

The work done in this thesis aim to describe the beamline compound with a prarametric probabilistic model. Parameter estimates are obtained using a non-linear least squares regression approach on both experimental and simulated data. The distributions and confidence intervals for the estimated parameters are constructed using the parametric bootstrap.

Acknowledgements

I would like to thank my supervisor Dragi Anevski at the Centre for Mathematical Sciences at Lund University as well as my external supervisors Kalliopi Kanaki and Richard Hall-Wilton of the Detector Group at the European Spallation Source (ESS).

In particular I would like to thank Kalliopi Kanaki for providing me with the data, both experimental and simulated, as well as for her patience and support in helping me understand the physics of this problem.

Contents

1 Introduction

The traditional neutron detector used today is a helium-3 filled gas detector with a single detection volume. Since the supply of this gas is scarce scientists are investigating alternative materials and designs to construct new detectors. At the European Spallation Source (ESS), located in Lund, a candidate for this new detector designs is being developed. In contrast to the single detection volume of todays detectors the new detector design consisting of a grid on detection cells placed in depth.

The new detector design has an advantage over the traditional as it gives information about the penetration depth of the neutron in the detector. This gives hope that the additional information about the penetration depth could be utilised to obtain information about the wavelength composition of the neutron beams used in neutron scattering experiments. The aim of this thesis is to make an initial attempt to model the wavelength composition of such beams, more exactly beams where monochromatic crystals are applied, as well as shine a light on difficulties combined with this problem. The work done in this thesis is part of a greater collaboration between ESS and the Centre for Mathematical Sciences at Lund University.

1.1 ESS

The European Spallation Source is a massive science and technology infrastructure projects being built today in Lund, Sweden. Planned to be operational in 2019, and the world's leading material research centre using neutrons by 2025, cf. [1]. The purpose with the facility is to provide neutrons for the study of materials on an atomic, or even deeper, level. It will be used in numerous fields from plastics and pharmaceuticals, to engines, and molecules. The facility will be used by around two to three thousand guest researchers each year from all over the world. Most of these will be based at universities and institutes, others within industry, cf. [1]. A conceptual picture over the ESS facility is presented in Figure 1.

The reason why yet another neutron facility is required is that most of the current ones are built with nuclear reactors as the neutron source. This technology has reached its maximum capacity and the development has stopped. ESS instead utilises spallation as neutron source. This is done by accelerating protons and colliding them with a heavy metal target. On impact the target expels a number of nucleons, among them neutrons at various velocities. They are then moderated, or slowed down, to a desirable energy range. Neutrons traveling along a specific direction then forms a beam or beamline that can be used to probe materials. When ESS is operational the beams will be around 30 times brighter than current facilities, cf. [1].

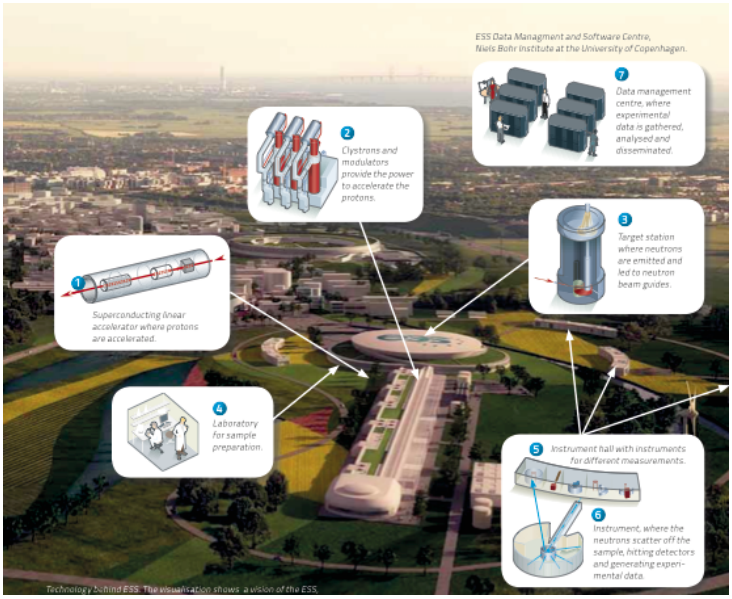

Figure 1: Conceptual picture over the ESS facility.

1.2 New detector design

Older facilities traditionally uses helium-3 (^{3}He) gas filled detectors because of its high neutron capture capacity, but due to the world wide ^{3}He shortage, cf. [2], other elements are being investigated to find a replacement.

One of the strongest candidates to replace ^{3}He is boron-10 (^{10}B) because of its similarities with ^{3}He in terms of neutron capture capacity, cf. [3]. In these detector designs thin layers of ^{10}B are coated onto a substrate blade, e.g. aluminium (Al). One alternative detector design, being developed at ESS, uses a number of ^{10}B, or rather B_4C, coated Al blades placed in depth, see Figure 2. This results in a number of detection volumes, or cells, in depth unlike ^{3}He detectors which only have one detection volume. In this thesis the additional depth dimension of the detector will be utilised in an attempt to obtain additional information about the beamline, more exactly its wavelength composition. A technique that reliably could extract this information would be of great help in the analysis of experimental data and thus contribute to the numerous fields where neutron spectroscopy is a useful tool, cf. [4], [5], [6] and [7].

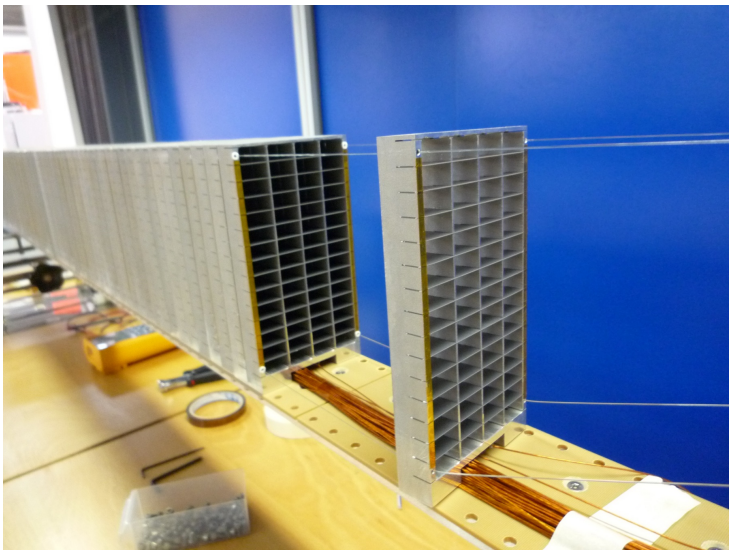

Figure 2: Prototype of the new detector design being developed at ESS. Relative the picture the neutron beam is incident form above. The detector can be made to cover a wide angle deviation of the scattered neutrons. Since each cell registers detections individually both the angle deviation and penetration depth of the scattered neutron is measured.

2 Physics background

This section covers some basic physics background in the conceptual understanding of neutron spectroscopy. For a more thorough introduction to the subject the reader is referred to Neutron scattering - A primer by Roger Pynn, cf. [8].

2.1 Why neutrons?

Light and x-rays together with electrons have proven to be quite successful as a tool to study surface properties and deeper structures of matter. However these techniques have some natural limitations when it comes to the study of the inner structures of bulk materials. One downside is that the wavelength of the radiation have to be of the same magnitude as the structure of interest, cf. [8].

When studying the interatomic distances of a bulk material with light, the limiting factor is its wavelength, about 10^{-6} m. It is several orders greater than a typical interatomic distance, in magnitude about 10^{-10} m. Instead x-rays can be used for this purpose. The interaction of interest is mainly scattering which, in this case, is an interaction between the x-rays and the electrons of the material. Heavy atoms, with a lot of electrons, scatter x-rays more efficiently than lighter atoms, with less electrons. This could make lighter atoms in a compound bulk material more or less invisible if heavier atoms dominate the interaction, making it very hard to say anything about the positioning of the lighter atoms. Electrons also have their drawbacks since they are electrically charged particles and interact strongly with electrons of the bulk itself. This makes them unsuitable for the study of the inner properties of such matter.

The neutron however is electrically uncharged and its electrical dipole moment, if it even exists, is too small to measure. This makes the neutron much more penetrative to matter than charged particles, since the neutron's electric interaction with matter is weak. Instead the main interaction will be with the nucleus via the strong nuclear force that has a range of a few fermi, 10^{-15} m. Compared to a typical inter-nuclei distance the spacing between centres of interaction is typically 100000 times greater than the centre itself, cf. [8]. As a consequence neutrons can penetrate deep into most bulk materials before any interaction occurs. A conceptual view over the scattering process for different projectiles is presented in Figure 3.

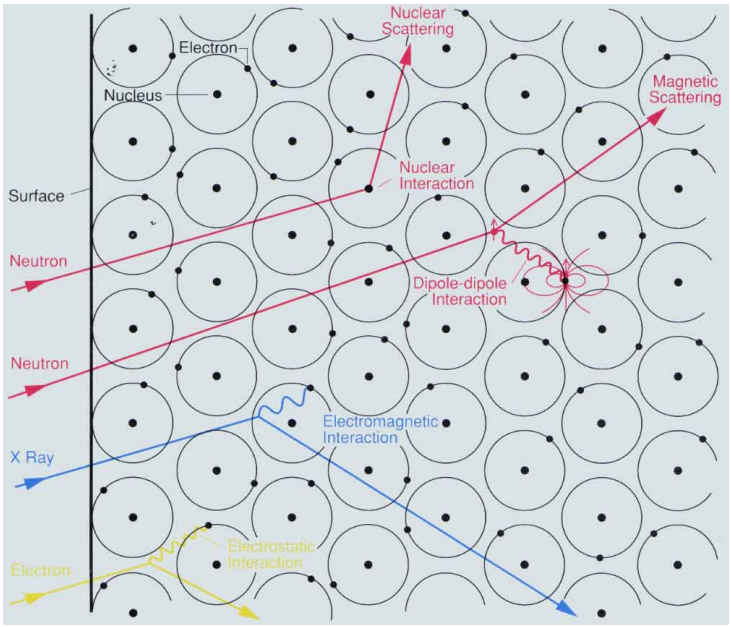

Figure 3: A schematic picture over scattering describing the interactions of the different projectiles. Yellow is the electron scattering, blue X-ray and red neutrons.

2.2 Scattering

Scattering is the interaction of interest in neutron spectroscopy. This can either be due to interaction between neutron and nucleus or neutron and the dipole moment of an unpaired neutron in matter. Here the concepts of scattered by nuclei will be addressed.

Neutrons used in scattering experiments have wavelengths, λ, around a few ångström, Å (10^{-10} m). Compared to the range of the strong nuclear force, in the region of 10^{-15} m, the wavelength that give rise to the scattering its huge. As seen by the neutron the nucleus is just a point, thus it can be viewed as a point scatterer, giving rise to isotropic scattering. This means that a neutron has equal probability to scatter at any angle from the target nucleus. Describing the neutron by its wave function this can be seen as a plane wave incident on the target nucleus that scatters the wave spherically.

As a beam of neutrons hits a sample they will interact with the nuclei of the matter and scatter, thus spherical wavefronts will spread from

the nuclei. The waves from each nucleus will interact with each other as they overlap. At some points they will reinforce one another and at others cancel out. This is the concept of interference. The constructive interference will not be possible for all directions but is dependent on the inner structure of the material itself. It is in these directions scattered neutrons will be observed.

Scattering of this type is called diffraction and the angle deviation between incident and scattered neutron is called the scattering angle, 2ϕ. Here ϕ is chosen as symbol instead of θ since θ is traditionally used as the unknown parameter vector in estimation problems. Possible scattering angles for neutrons with λ incident on a sample with parallel planes of planes of atoms at distance d is governed by Bragg's law, (1). Here n is an integer value.

$$n\lambda = 2d\sin\phi \tag{1}$$

Another way to characterise the scattering is by the scattering vector $\mathbf{Q}$. This is defined as the change in the wave vector between the incident and scattered neutron, $\mathbf{Q} = \mathbf{k} - \mathbf{k}'$. The wave vector is collinear with the velocity v and defined as (2).

$$\frac{h\mathbf{k}}{2\pi} = m\mathbf{v}. \tag{2}$$

Here h is the Planck constant and m the neutron mass. The product $m\mathbf{v}$ is the momentum of the neutron. The change in momentum in the scattering process would then be,

$$\frac{h}{2\pi}\mathbf{Q} = \frac{h}{2\pi}(\mathbf{k} - \mathbf{k}'). \tag{3}$$

If the scattering is elastic, i.e. no energy is exchanged between the neutron and nucleus the magnitude of the scattering vector is,

$$Q = 2k\sin\phi = \frac{4\pi\sin\phi}{\lambda}, \tag{4}$$

where k is the magnitude of the wave vector.

It is primarily the vector Q that is used in the analysis of experimental data to deduce the inner structure of the sample matter. For a compound sample this is not an easy task and can take considerable amount of time. This motivates the need of good knowledge of the beamline's wavelength composition which is focus of this thesis.

2.3 Cross section

An important parameter to describe neutron nuclei interaction is the cross section, c, which is measured in the unit barns (10^{-28} m^2). Here c is used to label the cross-section parameter instead of σ since σ is traditionally used as the symbol for standard deviation. It can be described as the effective area, of the nucleus, as seen by the neutron. If the neutron hits this area an interaction occurs with probability 1, otherwise 0. Each type of interaction has its own cross section, e.g. scattering, c_s, and absorption, c_a. They can be added up to obtain the total c of any of these interactions to occur, $c = c_a + c_s$, or be treated individually if only one of the possible interactions is of interest.

Since an interaction occurs if the neutron hits the effective area, the probability of a neutron nucleus interaction as a beam of incident neutrons fall upon a layer of atoms, can be described as, cf. [9],

$$p = \frac{n \cdot c}{A}. \tag{5}$$

Here p is the probability of an interaction, A is the area of the geometric cross section illuminated by the beam n the number of atoms in the this area.

In the estimation problem to come c_a, or the parametrisation $c_a(\lambda)$, is the relevant cross-section. The cross-section c_s is important in the understanding of the scattering experiment itself.

2.4 Crystal monochromators

One technique to make a selection of wavelength from a white neutron beam is to make use of monochromatic crystals. These crystals utilise diffraction to reflect neutrons of a given wavelength in the desired direction, depending on its orientation. As a beam, with a continuous distribution of wavelengths, falls upon parallel layers, or planes, of a crystal with an incident angle ϕ a wavelength λ will be diffracted at the same angle ϕ. Besides the crystal orientation, the wavelength diffracted also depends on the spacing of planes d of the crystal according to Bragg's law (1), as discussed in the section concerning scattering.

If there, for a given crystal orientation, exists a set of parallel planes with spacing d, and a beam, with a continuous distribution of wavelengths, falls upon the crystal with incident angle ϕ, a given wavelength λ will be reflected, according to Bragg's law. If the spacing of planes at this orientation is even denser, say $d/2, d/3, d/4, \ldots$ the crystal monochromator will also be able to reflect wavelengths $\lambda/2, \lambda/3, \lambda/4, \ldots$ at the same crystal orientation, cf. [10]. These wavelength contributions are regarded as contaminations and are referred to as second-order, third-order, forth-order, ... reflections, cf. [11]

2.5 Data collection

The data to analyse is produced at two different facilities as well as one simulated dataset. The first set of measurements comes from Helmholtz-Zentrum Berlin für Materialien und Energie (HZB), this dataset will be referred to as HZB. The second dataset is obtained from a new, ESS dedicated, beamline at the Norwegian Institutt for energiteknikk's (IFE).This dataset will be referred to as IFE. The last dataset is a simulated set of four measurement series.

The data collection is made with ^{3}He-gas filled detectors. The beamline is turned on and an initial measurement of the detection rate is made, i.e. the number of detected neutrons per second is measured. Then a B_4C coated Al blade is put in the path of the beamline, which is turned on, and another measurement is made. This is done for a set of B_4C coated blades to obtain a measurement series consisting of pairs (d_i, n_i), $i = 1, \dots k$. Here d_i is the total depth of B_4C at point i, n_i the registered detection rate and k the total number of measured pairs in the series. Each layer of B_4C has a thickness of 1 μm and the Al blades are 0.3 mm thick. The Al blades generally have a coating on each side. The number of B_4C layers used at each facility and for simulations are:

(i) 0 to 30 in even steps for the IFE measurements,

(ii) 0, 1, 2, 4, 6, 8, 10, 12, 14, 16, 18 and 20 for the HZB measurement,

(iii) 0 to 19 for the simulated data.

Before a measurement series is acquired a selection of wavelength is made. This is done either by a monochromator or a velocity filter consisting of a set of chopper discs. The five series of the IFE dataset and the first of HZB are made with a crystal monochromator as wavelength selector while the remaining measurements of HZB are acquired with a velocity filter. The simulated data is made to resemble monochromator filtered data. In Tables 1 and 2 the selected wavelength for each measurement series, of the experimental data, can be seen. Figure 4 shows the schematics of the experiment lineup after a wavelength selection has been made.

Table 1: Monochromator set λ, in Ångström, for the IFE dataset.

λ	0.88	0.94	1.12	1.54	2.41

Table 2: Selected λ, in Ångström, for the HZB dataset. All λ are selected via a velocity filter, except the first which is a monochromator set λ.

λ	3.35	4.5	4.6	5.27	6.48	6.8	7.92	9	10.97

In the analysis to come, focus will be on the experimental data that uses a crystal as monochromator. That is the IFE data in Figure 5 and the first, and only, HZB measurement series of this kind, displayed in Figure 6. These measurement series will be referred to as the crystal data or dataset. Finally Figure 7 is a plot over the simulated data.

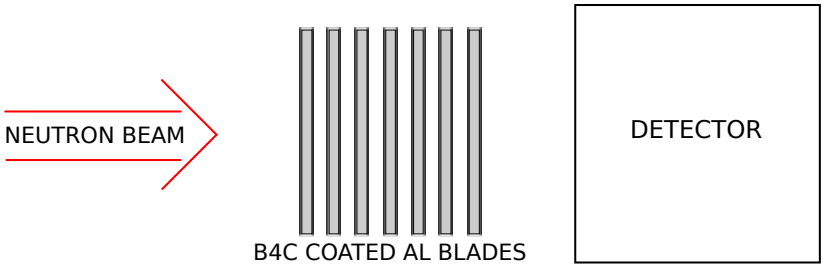

Figure 4: Schematics over experiment lineup after λ selection has been made.

As described in the section concerning crystal monochromators, the beam reflected by the crystal may contain contaminations to some extent. An account for possible wavelength content of the reflected beams is stated in Table 3.

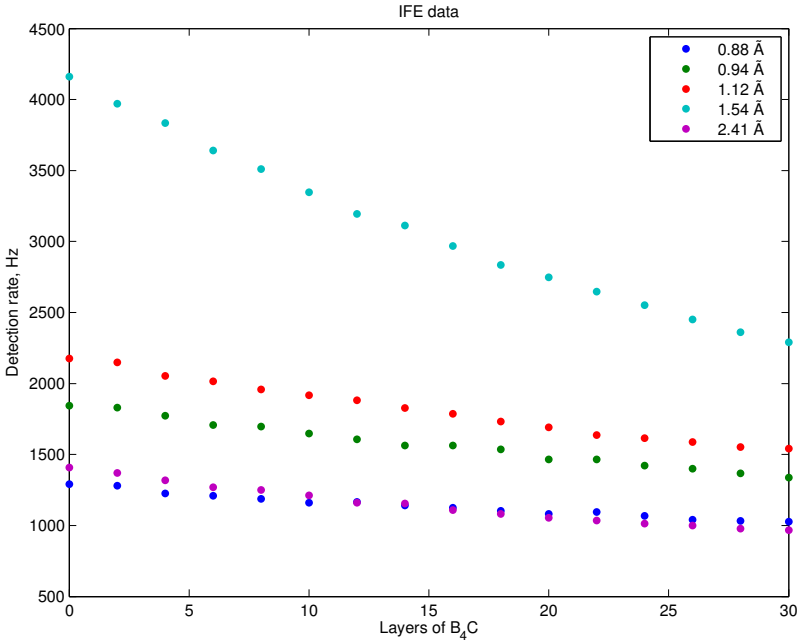

Figure 5: Experimental data of the IFE measurements. The legend displays the wavelength, in Ångström, that the crystal monochromator was set to reflect. From the plot it can be seen that measurement series with shorter wavelengths have flatter profiles.

Table 3: Wavelengths allowed by the crystal monochromator for each measurement series. The first column contains the wavelengths the crystal is set to reflect for each series.

0.88	λ		$\lambda/3$
0.94	λ	$\lambda/2$	$\lambda/3$
1.12	λ		$\lambda/3$
1.54	λ		$\lambda/3$
2.41	λ		$\lambda/3$
3.35	λ	$\lambda/2$	$\lambda/3$

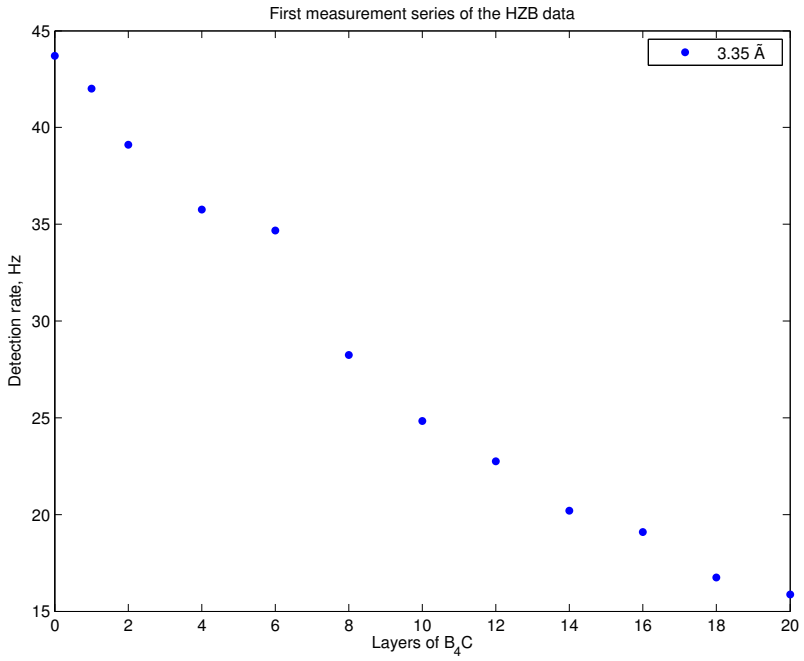

Figure 6: The only measurement series of the HZB dataset made with a crystal monochromator. Since the plot contains a single series it is easier to see the behaviour of the data. The measurements seems to follow an exponential decay with some points being slightly pushed up or down. The other series displays the same qualitative behaviour.

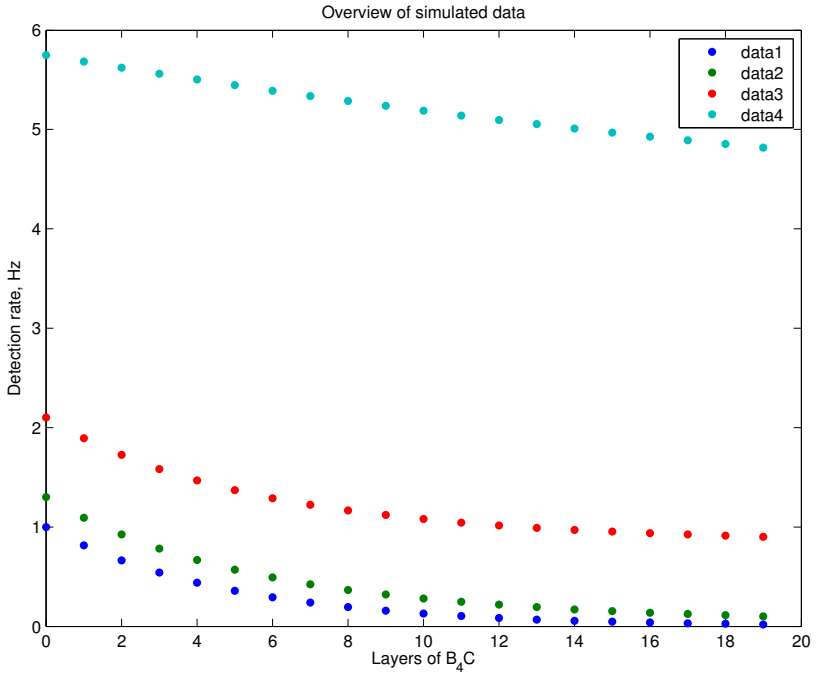

Figure 7: Simulated dataset consisting of four series produced to resemble data from a beam reflected by a crystal monochromator.

As mentioned earlier, the detectors used in the experiments are ^{3}He-gas filled detectors. The efficiency of such a detector depends on both the wavelength and the detectors gas pressure. At IFE a high pressure

detector is used while a low pressure detector is used at HZB, though no exact pressure for either of them can be confirmed hence their efficiencies are unknown. Figure 8 displays efficiency profiles for ideal detectors, only containing ^{3}He, for different pressures. The parametrisation of the efficiency for the ideal detector is provided by Kalliopi Kanaki at the detector department at ESS.

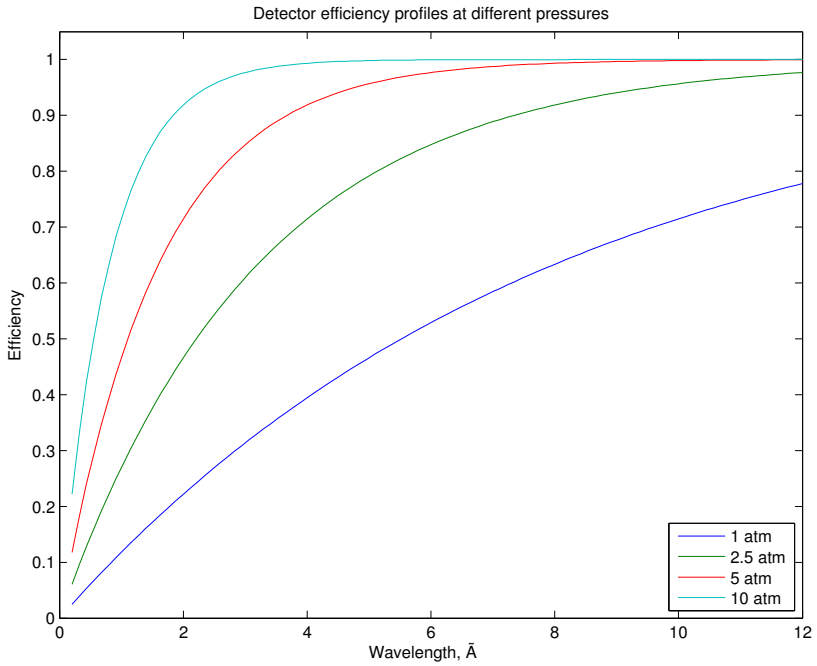

Figure 8: Detector efficiency as a function of λ for 2.5, 5 and 10 atm pressure. The profile of the IFE detector would resemble that of a high pressure detector while HZB would be more similar to the profile of a low pressure detector.

3 Problem formulation

In this section the physical understanding of neutron absorption will be transformed into a statistical regression model used to obtain estimates of the beamline composition. Details of how the models are constructed as well as parameters constraints of physical origin is discussed. Finally properties of the estimator and the parametric bootstrap, used to obtain confidence intervals, for the estimates are presented.

3.1 Mathematical modelling of absorption

For a flux of neutrons J, i.e. the intensity of incident neutrons given in Hertz per area unit, passing through an absorbing matter the remaining flux after depth x can be modelled by the absorption law, cf. [4],

$$J = J_0 e^{-c(\lambda) n_{at} x}. \tag{6}$$

Here J_0 denotes the initial flux, c the cross-section for absorption in the matter, λ the neutron wavelength and n the atomic density of the matter. Mathematically this is a deterministic model and can only be assumed correct when all relevant parameters are known.

If instead an initial rate of incident neutrons, N_0, is regarded the remaining rate of neutrons, n, after passing a depth x of absorbing matter can be modelled as,

$$n = N_0 e^{-c(\lambda) n_{at} x} + \varepsilon. \tag{7}$$

Here an additive error term, ε, has been added to the model. The error term ε can be considered as a stochastic variable with expected value 0 and error variance σ. The variance σ could be depth dependent, i.e. $\sigma = \sigma(x)$, or both depth and λ dependent, $\sigma = \sigma(x, \lambda)$. Allowing for both depth and λ dependence of the error variance (7) could then be written as,

$$n = N_0 e^{-c(\lambda) n_{at} x} + \varepsilon(x, \lambda). \tag{8}$$

The above equations hold for a beam of incident neutrons with one wavelength. It can be generalised to a discrete composition of wavelengths $\{\lambda_1, \lambda_2, \ldots\}$ with respective proportions $\{p_1, p_2, \ldots\}$ as follows,

$$\begin{aligned} n &= \sum_j p_j \left(N_0 e^{-c(\lambda_j) n_{at} x} + \varepsilon(x, \lambda_j) \right) \\ &= \sum_j p_j N_0 e^{-c(\lambda_j) n_{at} x} + \sum_j \varepsilon(x, \lambda_j) p_j \\ &= \sum_j p_j N_0 e^{-c(\lambda_j) n_{at} x} + \tilde{\varepsilon}(x), \end{aligned} \tag{9}$$

with

$$\tilde{\varepsilon}(x) = \sum_j \varepsilon(x, \lambda_j) p_j.$$

An even more general description is to allow for any continuos composition of wavelengths as,

$$
\begin{aligned}
n &= \int_{\Lambda} f(\lambda)\big(N_0 e^{-c(\lambda)n_{at}x} + \varepsilon(x,\lambda)\big)\mathrm{d}\lambda \\
&= \int_{\Lambda} f(\lambda) N_0 e^{-c(\lambda)n_{at}x}\mathrm{d}\lambda + \check{\varepsilon}(x),
\end{aligned}
\tag{10}
$$

with

$$
\check{\varepsilon}(x,\lambda) = \int_{\Lambda} f(\lambda)\varepsilon(x,\lambda)\big)\mathrm{d}\lambda.
$$

The composition of wavelengths is described by the non negative function $f(\lambda)$ defined on the space Λ with property

$$
\int_{\Lambda} f(\lambda)\mathrm{d}\lambda = 1.
$$

To take the model one step closer to what is actually observed the detector efficiency, ϵ, need to be included. This is a wavelength dependent parameter, thus $\epsilon = \epsilon(\lambda)$. This results in the following corrections to (8) - (10).

$$
n = N_0\epsilon(\lambda)e^{-c(\lambda)n_{at}x} + \varepsilon(x,\lambda), \tag{11}
$$

$$
n = \sum_j p_j N_0\epsilon(\lambda_j)e^{-c(\lambda_j)n_{at}x} + \tilde{\varepsilon}(x), \tag{12}
$$

$$
n = \int_{\Lambda} f(\lambda)N_0\epsilon(\lambda)e^{-c(\lambda)n_{at}x}\mathrm{d}\lambda + \check{\varepsilon}(x). \tag{13}
$$

As a final modification to the model a possible background contribution can be added if there are reasons to assume that the environment in an experimental setup contributes to the detection rates. This will be assumed to be a constant offset term independent of the other parameters in the model. Thus (11) - (13) receive the final modification as,

$$
n = N_0\epsilon(\lambda)e^{-c(\lambda)n_{at}x} + B + \varepsilon(x,\lambda), \tag{14}
$$

$$
n = \sum_j p_j N_0\epsilon(\lambda_j)e^{-c(\lambda_j)n_{at}x} + B + \tilde{\varepsilon}(x), \tag{15}
$$

$$
n = \int_{\Lambda} f(\lambda)N_0\epsilon(\lambda)e^{-c(\lambda)n_{at}x}\mathrm{d}\lambda + B + \check{\varepsilon}(x). \tag{16}
$$

Up to this point no assumptions is made on the distributions of the errors.

3.2 Parameterisation of c

Looking at experimentally determined cross-sections the relation between c and λ in the region of interest shows a strong linear behaviour. Therefore a linear model, see (17), is fitted to 42 cross- section data points by simple linear regression.

$$
c(\lambda) = \alpha + \beta \cdot \lambda \tag{17}
$$

The data is acquired from the National Nuclear Data Centre, NNDC, cf. [12], and is displayed, together with the linear fitted model, in Figure 9. Parameter estimates with corresponding 99% confidence interval is presented in Table 4. The fit is made to c in barn and λ in Ångström.

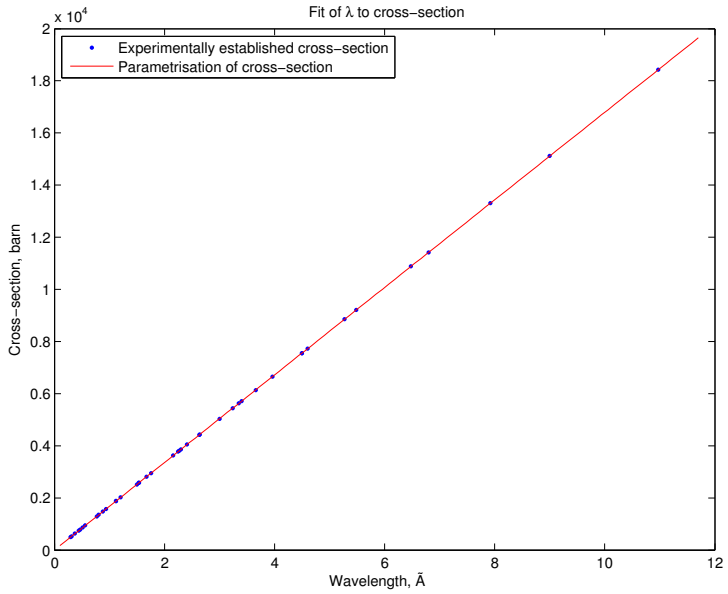

Figure 9: Linear model of $c(\lambda)$, in barn and λ in Ångström. A linear assumption on λ dependent c seem to be a reasonable assumption in this region.

Table 4: Parameter estimates of the linear fit of λ to $c(\lambda)$.

	Parameter estimate	99% confidence interval
$\hat{\alpha}$	-0.852	(-1.386, -0.319)
$\hat{\beta}$	1679.295	(1679.155, 1679.436)

3.3 Parameters and constraints

Given measurements,

$$(d_i, n_i), \quad i = 1, \ldots, k$$

of a model of the type described in (12) the aim is to estimate its unknown parameters. For $j = 1 \ldots, r$, the first set of unknowns would be the wavelength proportions, $\{p_1, \ldots, p_r\}$, with

$$p_j \in [0, 1]$$

such that

$$\sum_j p_j = 1.$$

Since no parameterisation of ϵ can be made, the efficiency will also have to be treated as unknown, with restriction $\epsilon(\lambda_j) > 0$, as well as N_0. The wavelength proportions p_j can therefore not be estimated directly since it will be impossible to separate it from the other unknown components of the exponential coefficients. This means that they will be estimated together as,

$$a_j = p_j N_0 \epsilon(\lambda_j). \tag{18}$$

Replacing the cross-section in (12) with its linear wavelength dependence gives the wavelengths, $\{\lambda_1, \ldots, \lambda_r\}$, as the second set of unknowns.

Consequently, the unknown parameters to estimate are $\{a_1, \ldots, a_r\}$, where

$$a_j > 0,$$

and $\{\lambda_1, \ldots, \lambda_r\}$, where

$$\lambda_j > 0.$$

Thus the unknown parameter vector is,

$$\theta = \big((a_1, \ldots, a_r), (\lambda_1, \ldots, \lambda_r)\big) = (\theta^{(1)}, \theta^{(2)}) \in \Theta = \Theta^{(1)} \times \Theta^{(2)}$$

with parameter space,

$$\begin{aligned} \Theta^{(1)} &= \{a \in \mathbb{R}^r : a_j > 0\} \\ \Theta^{(2)} &= \{\lambda \in \mathbb{R}^r : \lambda_j > 0\}. \end{aligned} \tag{19}$$

Including a background term, as in (15), the unknown parameter vector is extended to

$$\theta = (\theta^{(1)}, \theta^{(2)}, \theta^{(3)}) \in \Theta = \Theta^{(1)} \times \Theta^{(2)} \times \Theta^{(3)} \tag{20}$$

where,

$$\begin{aligned} \theta^{(3)} &= b \\ \Theta^{(3)} &= \{b \in \mathbb{R} : b > 0\}. \end{aligned}$$

Here, the constraints of the parameters are merely natural restrictions and no additional physical properties or assumptions of the experimental line-up have been included.

For a model described in (11) or (14) the unknown parameter vector has a slightly different composition. Instead of estimating λ, it is replaced with c, thus the unknown parameter vector for (14) becomes,

$$\theta = (a, c, b) = (\theta^{(1)}, \theta^{(2)}, \theta^{(3)}) \in \Theta = \Theta^{(1)} \times \Theta^{(2)} \times \Theta^{(3)} \tag{21}$$

with,

$$\begin{aligned}\Theta^{(1)} &= \{a \in \mathbb{R} : a > 0\} \\ \Theta^{(2)} &= \{c \in \mathbb{R} : c > 0\} \\ \Theta^{(3)} &= \{b \in \mathbb{R} : b > 0\}.\end{aligned}$$

For a model of the type described by (11), $\theta^{(3)}$ and $\Theta^{(3)}$ are excluded.

A possible assumption to make is that the wavelength proportions of the beamline after reflection by a crystal monochromator are ascending with wavelength, i.e.

$$\begin{aligned}p_r > \ldots > p_1 > 0, \\ \lambda_r > \ldots > \lambda_1 > 0.\end{aligned}$$

Looking at the detector efficiency profiles, in Figure 8, the probability of detecting a neutron increases with its wavelength, e.g. $\epsilon(\lambda) > \epsilon(\lambda/2)$. This implies that the parameters a_j, in (18), can be constrained as,

$$a_r > \ldots > a_1 > 0.$$

Imposing these constraints modifies (19) to the following parameter spaces,

$$\begin{aligned}\tilde{\Theta}^{(1)} &= \{a \in \mathbb{R}^r : a_r > \ldots > a_1 > 0, \ \ \forall a_j\} \\ \tilde{\Theta}^{(2)} &= \{\lambda \in \mathbb{R}^r : \lambda_r > \ldots > \lambda_1 > 0, \ \ \forall \lambda_j\}.\end{aligned} \tag{22}$$

This gives the resulting unknown parameter vector, including possible background term,

$$\begin{aligned}\tilde{\theta} &= \big((a_1, \ldots, a_r), (\lambda_1, \ldots, \lambda_r), b\big) \\ &= (\tilde{\theta}^{(1)}, \tilde{\theta}^{(2)}, \theta^{(3)}) \in \tilde{\Theta} = \tilde{\Theta}^{(1)} \times \tilde{\Theta}^{(2)} \times \Theta^{(3)}\end{aligned} \tag{23}$$

These constraints are mainly made to resemble properties of the crystal monochromator.

3.4 The estimation problem

A set of six models in total are formed and named M_1 up to M_6 respectively. All models, except M_6, are used in the analysis of the crystal data.

M_1 and M_2 are both formed as single wavelength models according to (24) and (25) respectively,

$$f_1(x_i|\theta_1) = a \cdot e^{-c \cdot x_i} + \varepsilon_i, \tag{24}$$

$$f_2(x_i|\theta_2) = a \cdot e^{-c \cdot x_i} + b + \varepsilon_i. \tag{25}$$

Model M_1 are based on (11) and M_2 on (14). The known parameters are grouped into a covariate vector as,

$$x_i = n_{at} \cdot d_i \cdot 10^{-24}.$$

Here, $n_{at} = 1.02 \cdot 10^{23}$ cm^{-3} is the atomic density of ^{10}B the B_4C coating. The factor 10^{-24} comes from the fact that n_{at} is given in cm^{-3} and 1 barn $= 10^{-24}$ cm^2, which is the unit of the c estimate. The factor d_i is total depth, in cm, of the B_4C layers up to point i.

The following models are constructed in an attempt to capture the behaviour of a beam reflected by a monochromatic crystal. These are models M_3 and M_4, in (26) and (27) based on (12) and M_5, in (28) is based on (15),

$$f_3(x_i|\theta_3) = a_1 e^{-c(\lambda)\cdot x_i} + a_2 e^{-c(\lambda/2)\cdot x_i} + a_3 e^{-c(\lambda/3)\cdot x_i} + \varepsilon_i, \tag{26}$$

$$f_4(x_i|\theta_4) = a_1 e^{-c(\lambda)\cdot x_i} + a_2 e^{-c(\lambda/3)\cdot x_i} + \varepsilon_i, \tag{27}$$

$$f_5(x_i|\theta_5) = a_1 e^{-c(\lambda)\cdot x_i} + a_2 e^{-c(\lambda/3)\cdot x_i} + b + \varepsilon_i. \tag{28}$$

A beam reflected from these crystals may contain contaminations of the form, $\lambda, \lambda/2, \lambda/3 \ldots$. Depending on the crystal and its orientation it is also possible that a $\lambda/3$ term is present while a $\lambda/2$ is not. Table 3 gives an account of the λ content allowed by the crystal for each series of the crystal dataset. As a consequence, these models only need to include one unknown λ, and fractions of the same.

In addition to the estimation based on the real data a simulation study is made to evaluate the methods. The simulated data is made to resemble that of a beam filtered by a crystal monochromator. Therefore the last model, M_6 in (29), based on (15), is

$$f_6(x_i|\theta_6) = a_1 e^{-c(\lambda)\cdot x_i} + a_2 e^{-c(\lambda/2)\cdot x_i} + a_3 e^{-c(\lambda/3)\cdot x_i} + b + \varepsilon_i. \tag{29}$$

For this data models M_1, M_3, M_4, M_5 and M_6 are used.

The resulting estimation problem will be exemplified through M_4. Given data (d_i, n_i), $i = 1 \ldots k$, the parameter estimator is defined as,

$$\hat{\theta}_4 = (\hat{a}_1, \hat{a}_2, \hat{\lambda}) = \underset{\theta \in \Theta^{(1)} \times \Theta^{(2)}}{\operatorname{argmin}} \sum_{i=1}^{k} \big(n_i - \mu_4(d_i|\theta_4)\big)^2 \tag{30}$$

Here $\mu_4(x_i|\theta_4)$ is the expectation of M_4 according to (31),

$$\mathbb{E}(M_4|x_i, \theta_4) = \mu_4(x_i|\theta_4) = a_1 \cdot e^{-c(\lambda)\cdot x_i} + a_2 \cdot e^{-c(\lambda/3)\cdot x_i} \tag{31}$$

The estimator $\hat{\theta}_4$ in (30) is called the non-linear least squares estimator. In general, the parameter vector that minimises the function is denoted by $\hat{\theta}_{est}$. If possible, the sum of squares can be differentiated and the minimum obtained analytically that way. However, even though the sum is differentiable, no analytical solution to the minimisation of the sum of squares can be found in this case. Instead a numerical minimiser is used to calculate $\hat{\theta}_{est}$. The minimiser used utilises an Active-set method. Details of an algorithm of this kind is well described in optimisation literature, for instance in cf. [13].

Since $\hat{\theta}_{est}$ cannot be found explicitly the possibility of convexity of the minimisation problem becomes an important property to investigate. When the target function, i.e. the function to be minimised, is convex any minimum found will be the only minimum and thus global. If the target function would be convex with a minimum in the parameter space this minimum would be global and therefore the optimal point. If the global minimum is located outside the parameter space the optimal point

for the minimisation problem will be found on the border. Alternatively, if the target function is convex on the parameter space any minimum found therein will be optimal within this space. First convexity of a single term is studied,

$$\big(n_i - \mu_4(d_i|\theta_4)\big)^2.$$

For a general case applicable to the models described above this can be written as (32). This function will be convex if its Hessian, (33), is positive semi-definite, cf. [13]. The function to be analysed is,

$$g_i(a,c) = \big(n_i - a \cdot e^{-c}\big)^2, \tag{32}$$

with Hessian,

$$\mathbf{H} = \begin{pmatrix} \frac{\partial^2 g_i}{\partial a^2} & \frac{\partial^2 g_i}{\partial a \partial c} \\ \frac{\partial^2 g_i}{\partial a \partial c} & \frac{\partial^2 g_i}{\partial c^2} \end{pmatrix} \tag{33}$$

If the determinant of the Hessian is greater than or equal to zero it is a positive semi-definite matrix hence the function $g(a,c)$ is convex. The value of x_i can therefore be fixed to 1 in (32) since it is a positive constant and will not effect the sign of the determinant. The partial derivatives in the Hessian and its determinant are given by (34) - (37),

$$\frac{\partial^2 g_i}{\partial a^2} = 2e^{-2c}, \tag{34}$$

$$\frac{\partial^2 g_i}{\partial a \partial c} = -2e^{-2c}a + 2(n_i - ae^{-c})e^{-c}, \tag{35}$$

$$\frac{\partial^2 g_i}{\partial c^2} = 2e^{-2c}a^2 - 2(n_i - ae^{-c})ae^{-c}, \tag{36}$$

$$\det \mathbf{H} = -4e^{-2c}(-n_i + 2ae^{-c})(-n_i + ae^{-c}). \tag{37}$$

Since the parameters a and c are positive constants the determinant of (37) cannot be guaranteed to be non-negative. Thus the individual terms $g_i(a,c)$ in the sum (30) cannot be assumed convex in a and c. Therefore there is no guarantee that the sum is convex. This means that the minimisation problem is not convex on the parameter space and convergence to an optimal minimum cannot be ensured. As a consequence the solution obtained may be a local minimum and thus not the optimal point.

Conditions for asymptotic consistency of the non-linear least squares estimator is covered in [14]. These conditions have not been studied in detail for the specific estimation problem in this thesis. Therefore no guarantee for asymptotic consistency of the estimator can be made.

3.5 Bootstrap

Since no assumptions on the distribution of the errors can be made the distributions of the estimates are unknown. Therefore confidence intervals for the parameter estimates have to be created in an alternative manner. Here a parametric bootstrap scheme will be utilised to obtain distributions of the estimates and thereby confidence intervals.

Generally knowledge about the distribution of the data is needed in order to say anything about the distribution of $\hat{\theta} - \theta$, where $\hat{\theta}$ is the estimator and θ the true parameter value. This distribution contains all

information needed to analyse the accuracy of the estimator, e.g. values of quantiles in order to construct confidence intervals, and depends on the distribution of the original data sample.

In this case the distribution connected with the observations is the distribution of the errors, F. This is unknown but can be estimated as $\hat{F}$, given original data. If it can be assumed that $\hat{\theta}$ depends on $\hat{F}$ in the same manner as θ depends on F, both $\hat{\theta}^* - \hat{\theta}$ and $\hat{\theta} - \theta$ converges to the same distribution hence $\hat{\theta}^* - \hat{\theta}$ can be used as an estimator of the latter. $\hat{\theta}^*$ is calculated in the same way as $\hat{\theta}$ but with observations from $\hat{F}$ instead of F as $\hat{\theta}$, cf. [15].

To describe the above statements more exactly $\sqrt{k}(\hat{\theta}_k - \theta)$, where $\hat{\theta}_k$ are the parameter estimates obtained from k observations, is assumed to converge to a stochastic variable Z_F as,

$$\sqrt{k}(\hat{\theta}_k - \theta) \xrightarrow{\mathcal{L}} Z_F.$$

Here, Z_F is dependent on the distribution F linked to the observations and $\mathcal{L}$ means that the convergence is in distribution. The expression $\sqrt{k}(\hat{\theta}_k^* - \hat{\theta})$, where $\hat{\theta}$ now is a non-stochastic vector conditioned on the observations, then also converges to Z_F as,

$$\sqrt{k}(\hat{\theta}_k^* - \hat{\theta}) \xrightarrow{\mathcal{L}^*} Z_F.$$

Here $\mathcal{L}^*$ mean that the the above expression converges in distribution conditioned on the observations almost surely, cf. [15].

An estimator for the ξ_α quantile of $\hat{\theta} - \theta$ is seen below in (38). The quantile estimate $\hat{\xi}_\alpha$ is obtained as the smallest value of x that fulfils the inequality.

$$\mathbf{P}\left(\hat{\theta}^* - \hat{\theta} \leq x | \hat{F}\right) \geq 1 - \alpha \tag{38}$$

When $\hat{F}$ is a good estimate of the true distribution F the bootstrap estimates of the quantile should be close to the true value, e.g. (39) should hold.

$$\mathbf{P}\left(\hat{\theta} - \theta \leq \hat{\xi}_\alpha | \hat{F}\right) \approx 1 - \alpha \tag{39}$$

Intervals with asymptotic confidence level $1-\alpha-\beta$ can thus be obtained as,

$$[\hat{\theta} - \hat{\xi}_\alpha,\ \hat{\theta} - \hat{\xi}_{1-\beta}], \tag{40}$$

since,

$$\mathbf{P}\left(\hat{\xi}_{1-\beta} \leq \hat{\theta} - \theta \leq \hat{\xi}_\alpha\right) = \mathbf{P}\left(\hat{\theta} - \hat{\xi}_\alpha \leq \theta \leq \hat{\theta} - \hat{\xi}_{1-\beta}\right) = 1-\alpha-\beta. \tag{41}$$

As used in the work done in this thesis $\hat{\theta}$ is bootstrapped rather than $\hat{\theta} - \theta$ and the estimated quantiles, $\hat{\zeta}_\alpha$, are obtained as the smallest value of x that fulfils the inequality of (42)

$$\mathbf{P}\left(\hat{\theta}^* \leq x | \hat{F}\right) \geq 1 - \alpha \tag{42}$$

This is referred to as Efron's percentile method and the corresponding confidence interval is, se also (39) and (40),

$$[\hat{\zeta}_{1-\beta},\ \hat{\zeta}_\alpha] = [\hat{\theta} + \hat{\xi}_{1-\beta},\ \hat{\theta} + \hat{\xi}_\alpha]. \tag{43}$$

In this case the bootstrap for a regression model is used. Given the model,

$$y_i = m_\theta(x_i) + \varepsilon_i,\ \theta \in \Theta,$$

the observations y_i are used to estimate parameters θ as $\hat{\theta}$. This gives the estimated points as,

$$\hat{y}_i = \hat{m}_{\hat{\theta}}(x_i),$$

and the residuals are formed,

$$e_i = \hat{\varepsilon}_i = y_i - \hat{m}_{\hat{\theta}}(x_i).$$

The bootstrap sample is now sampled from these residuals.

The bootstrap algorithm used in this case is described in full detail below, cf. [16].

1. Form parameter estimates, $\hat{\theta}_{est}$, on the original data sample, (x_i, n_i) $i = 1, \ldots, k$. Calculate the fitted data points $\mu(x_i|\hat{\theta}_{est})$. Use the reconstructed points to calculate the residuals,

$$e_i = n_i - \mu(x_i|\hat{\theta}_{est}),\ \ i = 1, \ldots, k.$$

2. Draw k points with replacement from the residuals, $(e_1^*, \ldots, e_k^*)$. This is a bootstrapped residual sample. Add the bootstrapped residuals to the fitted function values to form a bootstrapped data sample,

$$n_i^* = \mu(x_i|\hat{\theta}_{est}) + e_i^*,\ \ i = 1, \ldots, k.$$

3. Form new parameter estimates, $\hat{\theta}_b^*$, on the bootstrapped data sample and store the results.

4. Repeat step 2. and 3. for $b = 1, \ldots, B$, for a large B.

The algorithm gives a large set of bootstrapped parameter estimates $(\hat{\theta}_1^*, \ldots, \hat{\theta}_B^*)$. By sorting the individual parameter estimates in ascending order, e.g. $(\hat{\lambda}_{(1)}^*, \ldots, \hat{\lambda}_{(B)}^*)$, a bootstrap estimate of the distribution of the estimate is obtained. Quantiles can be acquired from this distribution to construct confidence intervals.

Using this technique imposes some implicit assumptions on the errors and data described below:

(i) In step 2 a bootstrapped residual sample is randomly drawn, with replacement, from the original residuals and then added to the fitted data points. This means that any residual value can be added to any fitted point. The implication of this procedure is that the errors are assumed to be independent and identically distributed. In particular this means that their variance is constant.

(ii) The way of obtaining the residuals in step 1 assumes that the given parametric model is correct for the data, cf. [16].

An important remark to make here is that the properties of the bootstrap estimator discussed above are asymptotic. As used on the data at hand, where the IFE data consists of 16 data points for each series and the HZB data of only 12 points, these asymptotic properties cannot be guaranteed. However, since no assumption on the distribution of the errors is made the distribution of the estimator remains unknown and thus the bootstrap provides some useful information.

4 Results

Here the resulting parameter estimates and model fits will be presented. Firstly, parameter estimates and model fits on the simulated data are displayed. Then results for the single λ models, M_1 and M_2, on experimental data are presented. Lastly, resulting estimates for models adapted to crystal monochromator data, M_3, M_4 and M_5, on corresponding experimental data are visualised.

4.1 Simulated data

For the simulated data the models M_1 and $M_3 - M_6$ were evaluated without any prior knowledge of λ composition. The fitted models are then analysed and the best fit is selected as the most probable model for the data. Since this is a simulated dataset ϵ is fixed to one for all λ. Another important remark is that the data is generated without errors. Therefore a perfect fit is theoretically possible.

The data consists of four series. For these simulations the models M_6, M_2, M_5 and M_4 where deemed to give the best fit, respectively. Table 5 gives an overview of the parameter estimates for the respective model and series. Table 6 displays the parameters used to produce the data

Table 5: Parameter estimates for the model that produced the best fit for each series of the simulated data. The parameters estimated are those of respective model described in (29), (25), (28) and (27) except for (29) where c has been replaced with $c(\lambda)$.

	$\hat{a}_1$	$\hat{a}_2$	$\hat{a}_3$	$\hat{b}$	$\hat{a}_1 + \hat{a}_2 + \hat{a}_3 + \hat{b}$	$\hat{\lambda}$
M_1	0.9997	0.0000	0.0000	0.0000	0.9997	12.0010
M_4	0.9994	0.3005	0.0000	0.0000	1.2999	12.0065
M_5	1.0031	0.2959	0.0000	0.8006	2.0996	11.9651
M_6	0.9665	0.4667	0.9838	3.3330	5.7500	2.5225

Table 6: Parameters used to simulate the data. The parameter notation corresponds to that of M_6, M_2, M_5 and M_4.

	a_1	a_2	a_3	b	$a_1 + a_2 + a_3 + b$	λ
Data 1	1	-	-	-	1	12
Data 2	1	0.3	-	-	1.3	12
Data 3	1	0.3	-	0.8	2.1	12
Data 4	0.4	1.7	0.1	3.55	5.75	3

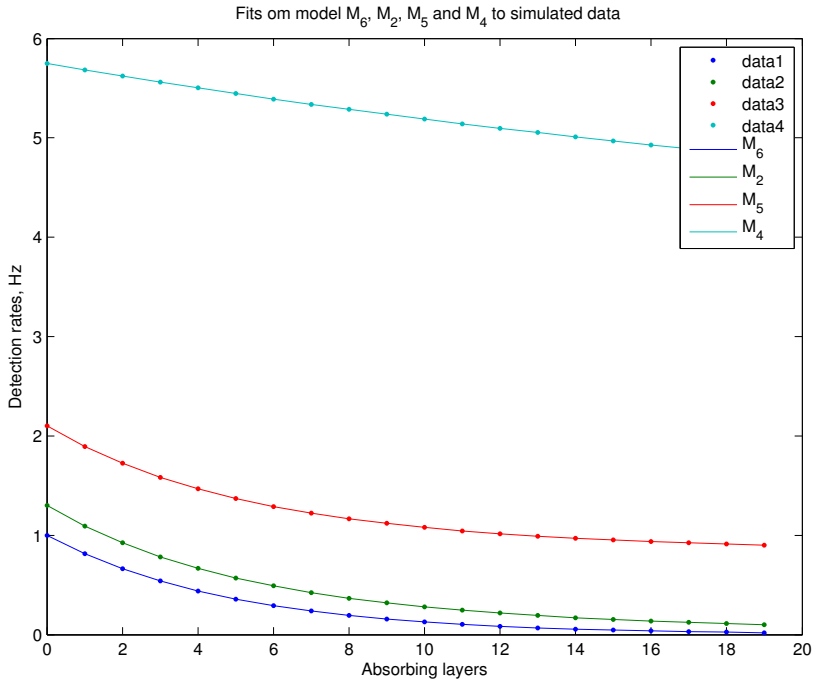

Figure 10: Simulated data along with the best fit for each series.

4.2 Single λ models

In this section results for the single wavelength models on the measurement series acquired with crystal monochromators will be presented. The estimations are made with the constraints in (21). Since the cross-section, c, is estimated instead of the wavelength Table 7 gives the relation between c and λ for each series.

Table 7: Wavelength with corresponding cross-section, column wise.

λ	0.88	0.94	1.12	1.54	2.41	3.35
$c(\lambda)$	1477	1578	1880	2585	4044	5625

In Figure 11 the cross-section estimates of M_1 and M_2, on the crystal dataset, are displayed. The M_2 estimates has a lot wider and skewer confidence bounds than those of M_1. The relative deviation of the point estimates and the expected cross-sections, as determined by the crystal orientation, is visible in Figure 12. Bootstrap distributions of estimated cross-sections for the third measurement series of IFE is displayed in Figure 13. Remaining distributions have similar shapes.

Figure 14 contains a plot of the a parameter estimates of M_1 and M_2 with 95% confidence bounds as well as a similar plot for the b estimates of M_2. Bootstrap distributions for these parameter estimates for the third measurement series of IFE is given in Figure 15.

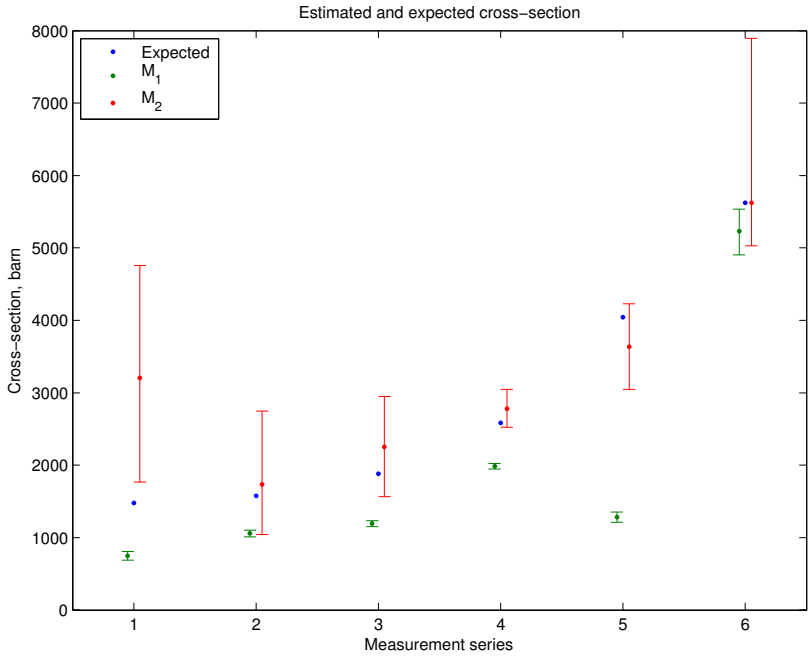

Figure 11: Estimated cross-sections of model M_1 and M_2 for all IFE and the first HZB measurement series, together with cross-sections corresponding the crystal selected λ of each series. The estimates are plotted with a 95% bootstrap confidence interval with 10000 bootstrap samples.

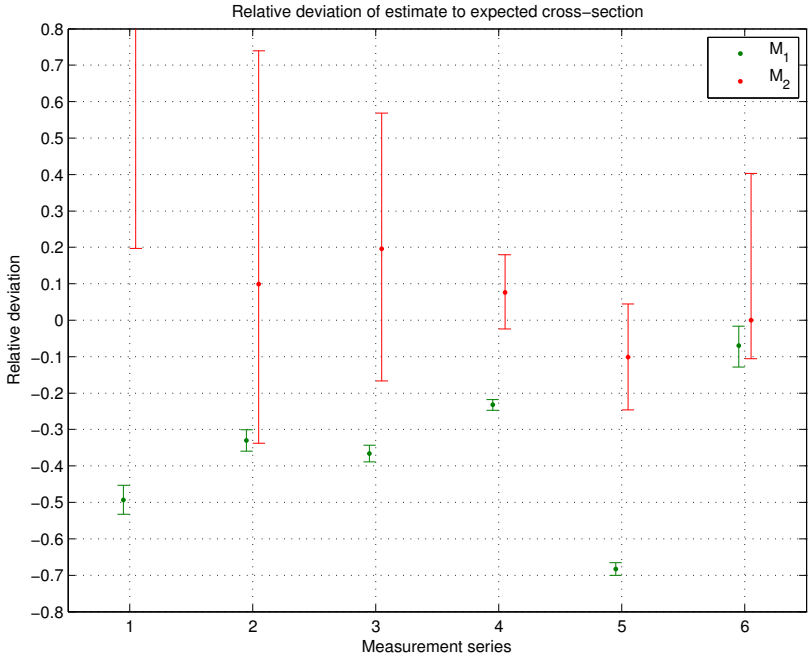

Figure 12: Relative deviation of c estimates to c corresponding the crystal selected λ of each series.

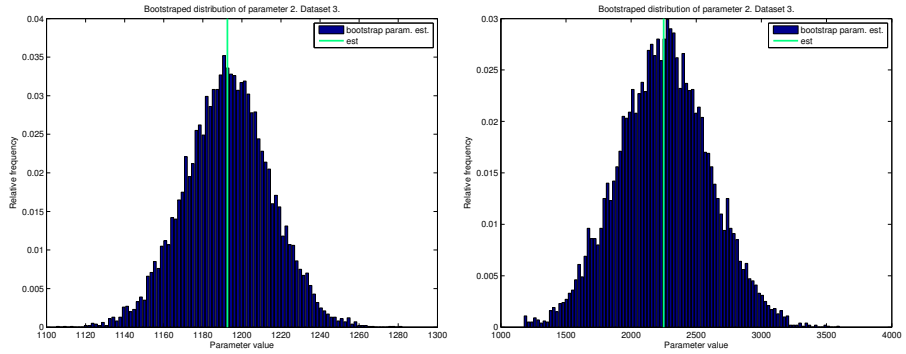

(a) Bootstrap distribution for $\hat{c}$ of M_1 (b) Bootstrap distribution for $\hat{c}$ of M_2

Figure 13: The bootstrap distributions of $\hat{c}$ of M_1 and M_2 for the third series of IFE. The estimates are marked as green vertical lines in the plots.

From Figure 13 it can be seen that the distributions of $\hat{c}$ for M_1 and M_2 seem quite symmetric. The distributions of the estimates for the other measurement series show the same behaviour.

In Figure 14 a estimates of M_1 has a lot narrower confidence bounds than those of M_2. The right plot displays the b estimates with relatively large bounds.

Table 8: Parameter estimates of M_1 on crystal data.

$\hat{a}$	$\hat{\lambda}$
1274.267	747.926
1844.675	1057.311
2170.578	1192.588
4129.226	1983.924
1387.436	1282.938
44.122	5230.547

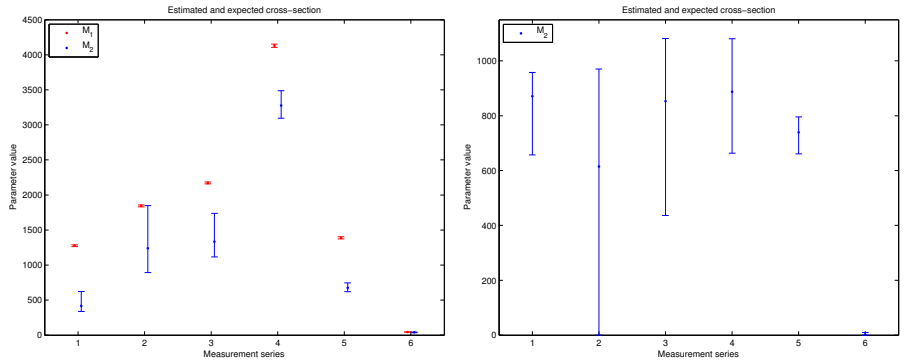

(a) Estimates of a parameters of M_1 and M_2 with 95% bootstrap confidence bounds.

(b) Estimate of b parameters of M_2 with 95% bootstrap confidence bound.

Figure 14: The left plot shows the a estimates of M_1 and M_2 on all crystal series with 95% confidence interval.

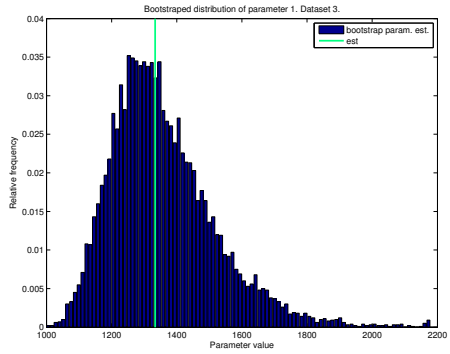

(a) Bootstrap distribution for $\hat{a}$ of M_2

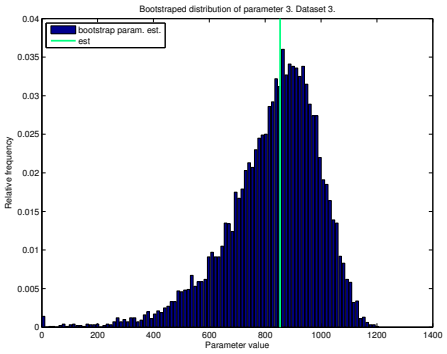

(b) Bootstrap distribution for $\hat{b}$ of M_2

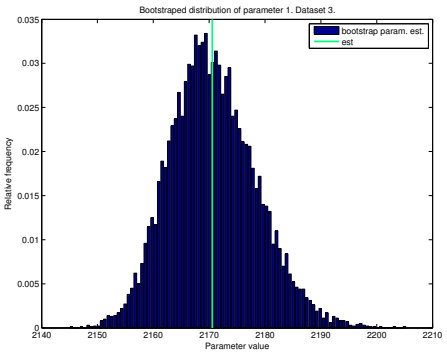

(c) Bootstrap distribution for $\hat{a}$ of M_1

Figure 15: Bootstrap distributions of $\hat{a}$ and $\hat{b}$ of M_2 and $\hat{a}$ of M_1, for the third series of IFE.

In the figure above it can be seen that the distributions of the M_2 a and b estimates are slightly skew while the distribution of $\hat{a}$ of M_1 is almost symmetric. The distributions of the estimates for the other measurement series show the same behaviour.

Table 9: Parameter estimates of M_2 on crystal data..

$\hat{a}$	$\hat{b}$	$\hat{\lambda}$
419.439	870.616	3204.843
1237.701	615.113	1734.993
1333.984	853.152	2249.389
3276.261	887.228	2781.851
673.848	739.165	3634.287
42.365	1.900	5625.016

4.3 Models for crystal data

Parameter estimations of models M_3 - M_5 where performed on the crystal data with the constraints of both (20) and (23). Results for estimations with the lesser constraints, (20), are presented under this section followed by an overview of the more restricted estimates in next section. Table 10 gives an overview of the crystal selected wavelengths and the detection rate of each measurement series with no blades in the beam.

Figure 16 gives the λ estimates along with 95% bootstrap confidence intervals for M_3-M_5 on the crystal data, while Figure 17 gives the point estimates relative deviation to crystal selected λ.

Tables 11, 12 and 13 shows all parameter estimates for M_3, M_4 and M_5 respectively.

Table 10: Count rate with no blades in the beamline and crystal monochromator set wavelength.

λ	0.88	0.94	1.12	1.54	2.41	3.35
0 layer rate	1292	1844	2175	4162	1409	43.7

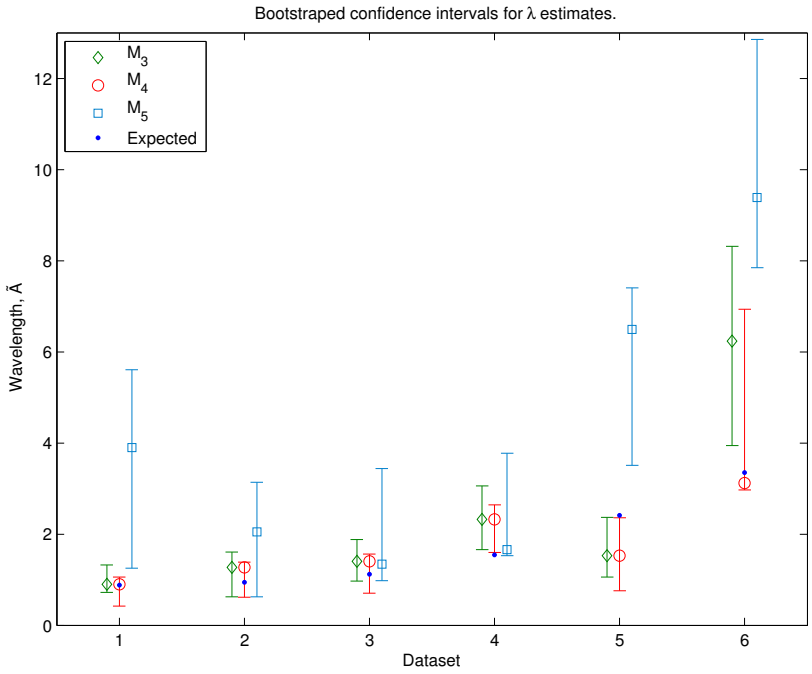

Figure 16: λ estimates of model $M_3 - M_5$ for the crystal data, together with corresponding 95% bootstrap confidence bounds produced with 10000 bootstrap samples.

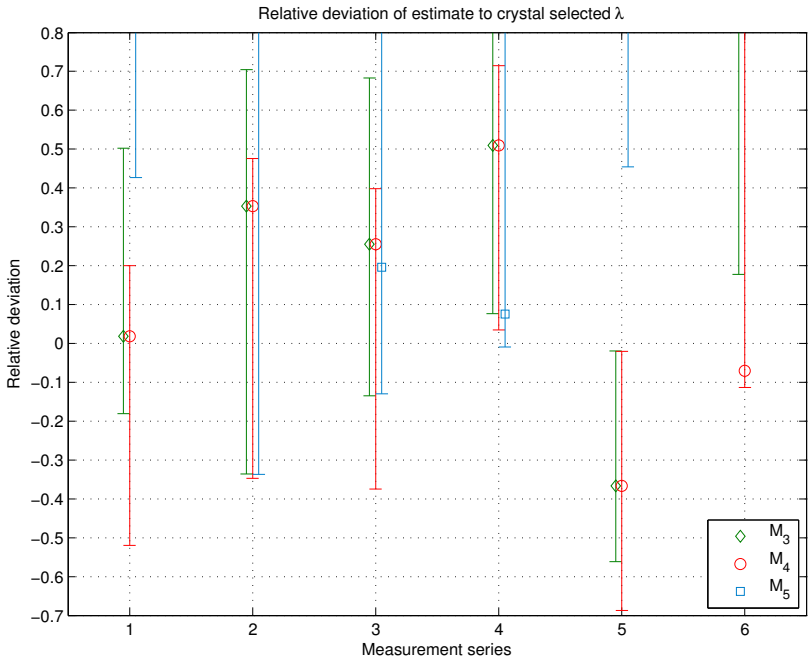

Figure 17: Relative deviation of λ estimates to crystal selected λ of each series. Point estimates of M_5 fall outside the plot except for the third and forth measurement series of crystal data but all lower bounds are visible.

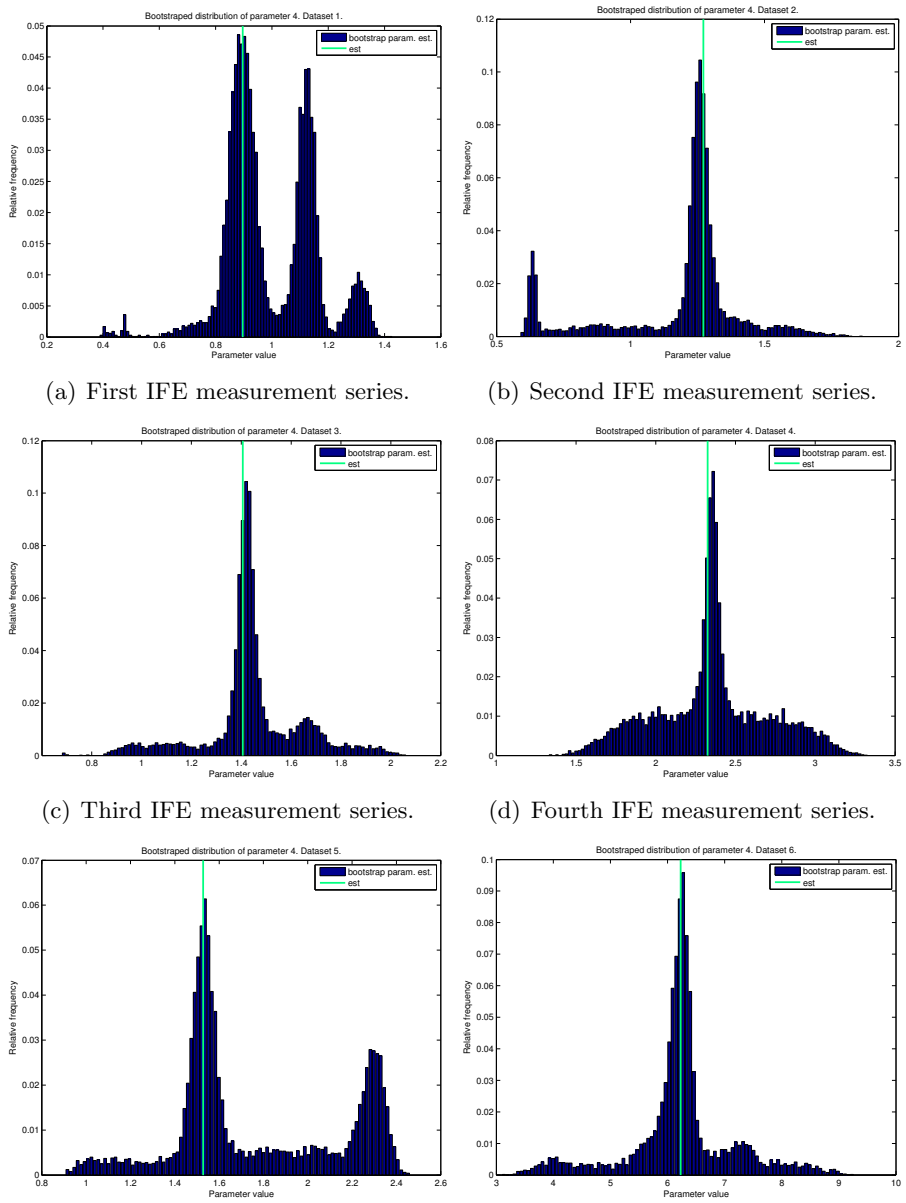

(a) First IFE measurement series.

(b) Second IFE measurement series.

(c) Third IFE measurement series.

(d) Fourth IFE measurement series.

(e) Fifth IFE measurement series.

(f) First HZB measurement series.

Figure 18: Distribution of λ estimates of M_3 for crystal data. Some plots displays more than one peak.

Looking at the plots of Figure 18 the peaks are being quite symmetric. This look resembles a sum of normal or at least unimodal distributions.

Table 11: Parameter estimates of M_3 for the crystal data.

$\hat{a}_1$	$\hat{a}_2$	$\hat{a}_3$	$\hat{a}_1 + \hat{a}_2 + \hat{a}_3$	$\hat{\lambda}$
352.123	0.000	923.971	1276.094	0.896
523.535	0.000	1325.608	1849.143	1.272
662.381	0.000	1514.889	2177.269	1.406
1399.996	0.000	2759.398	4159.394	2.325
419.739	0.000	973.069	1392.808	1.527
0.000	44.123	0.000	44.123	6.231

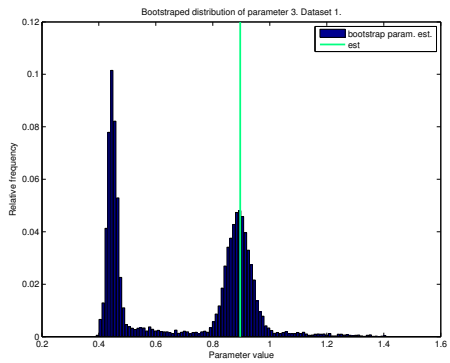

(a) First IFE measurement series.

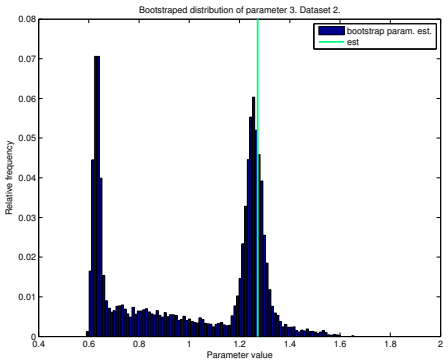

(b) Second IFE measurement series.

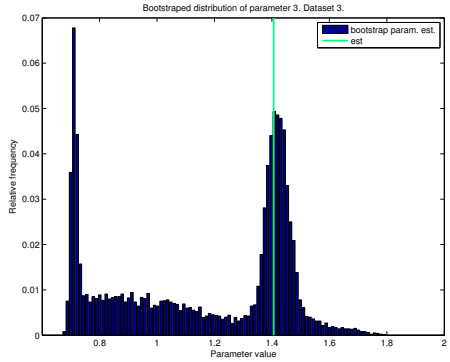

(c) Third IFE measurement series.

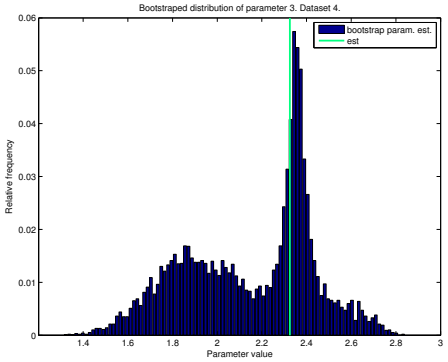

(d) Fourth IFE measurement series.

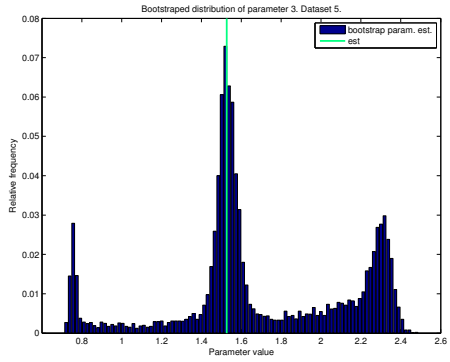

(e) Fifth IFE measurement series.

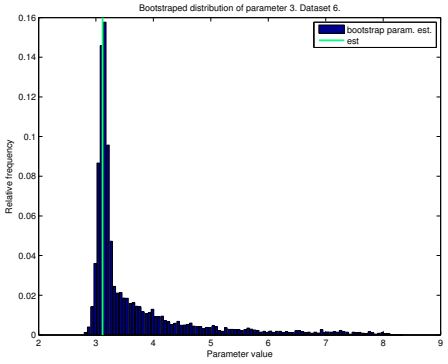

(f) First HZB measurement series.

Figure 19: Distribution of λ estimates of M_4 for crystal data.

In Figure 19 some plots displays more than one peak and similar to Figure 18 these plots have a look of a sum of unimodal densities.

Table 12: Parameter estimates of M_4 for the crystal data.

$\hat{a}_1$	$\hat{a}_2$	$\hat{a}_1 + \hat{a}_2$	$\hat{\lambda}$
352.111	923.984	1276.094	0.896
523.528	1325.615	1849.143	1.272
662.366	1514.903	2177.269	1.406
1400.031	2759.363	4159.394	2.325
419.737	973.070	1392.808	1.527
44.122	0.000	44.122	3.115

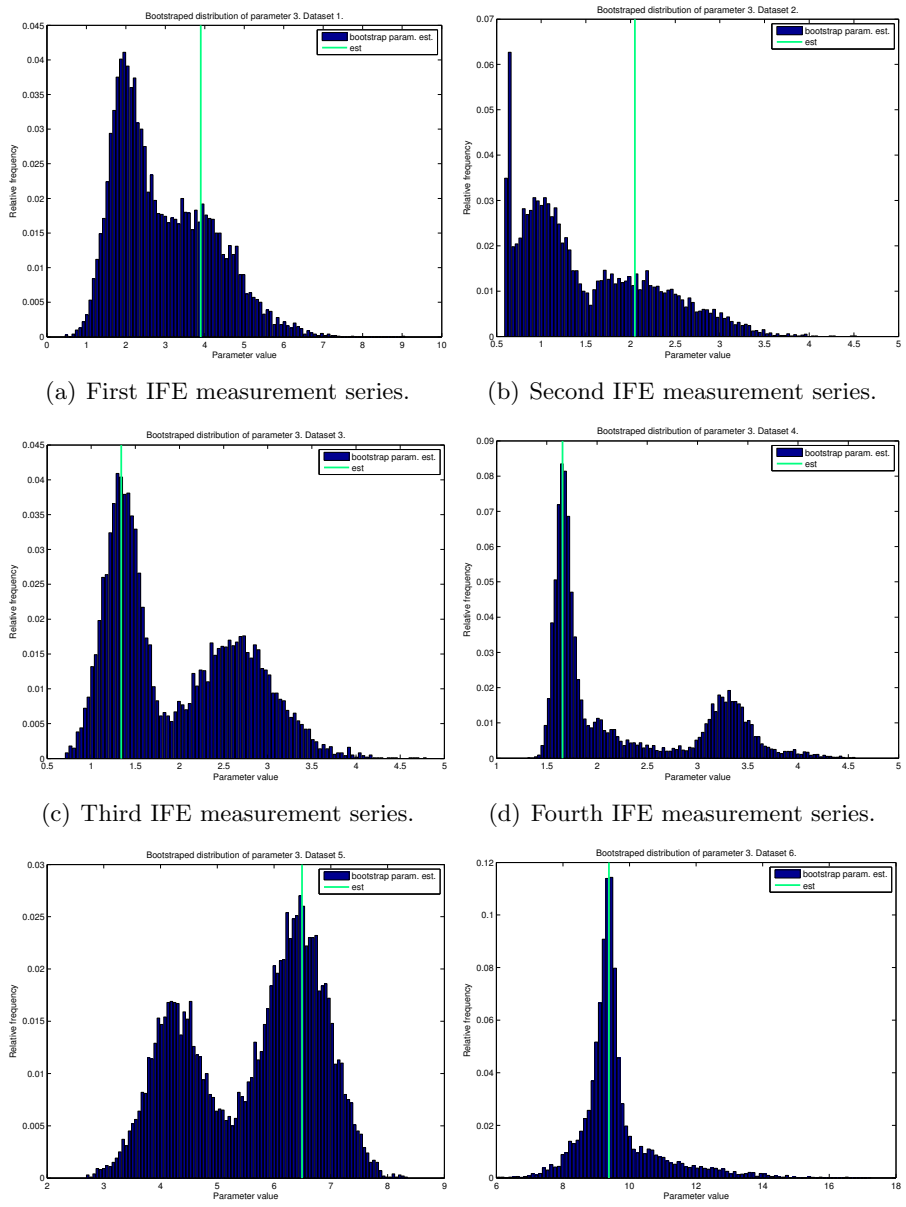

(a) First IFE measurement series.

(b) Second IFE measurement series.

(c) Third IFE measurement series.

(d) Fourth IFE measurement series.

(e) Fifth IFE measurement series.

(f) First HZB measurement series.

Figure 20: Distribution of λ estimates of M_5 for crystal data.

Figure 20 displays plots with wider peaks in the distributions of $\hat{\lambda}$ than those of Figure 18 and 19 . The tendencies of a mix of unimodal densities are present here as well.

Table 13: Parameter estimates of M_5 for the crystal data.

$\hat{a}_1$	$\hat{a}_2$	$\hat{b}$	$\hat{a}_1 + \hat{a}_2 + \hat{b}$	$\hat{\lambda}$
79.938	398.823	812.327	1291.088	3.897
207.920	1268.950	376.398	1853.268	2.048
1333.982	0.000	853.154	2187.136	1.340
3276.261	0.000	887.227	4163.489	1.657
0.000	673.847	739.165	1413.012	6.494
0.000	44.025	0.104	44.129	9.381

4.4 Models for crystal data with order constraints

Hereunder the results for parameter estimations of models M_3 - M_5, on the crystal data, with order constraints (23) follows.

Figure 21 gives the λ estimates along with 95% bootstrap confidence intervals for M_3-M_5 on the crystal data, while Figure 22 gives the point estimates relative deviation to crystal selected λ.

Figures 23 - 25 displays the bootstrap distributions of $\hat{\lambda}$ for M_3 - M_5. In general their appearance resemble that of corresponding plots in Figures 18 - 20.

Tables 14, 15 and 16 shows all parameter estimates for M_3, M_4 and M_5 respectively.

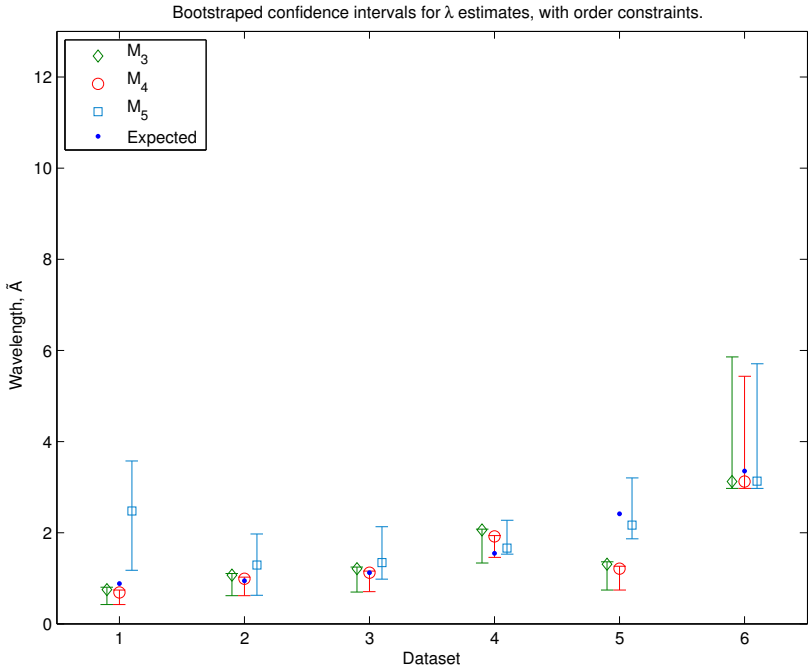

Figure 21: Estimates of λ for model $M_3 - M_5$ for the crystal data, with order constraints according to (23), together with corresponding 95% bootstrap confidence bounds produced with 10000 bootstrap samples.

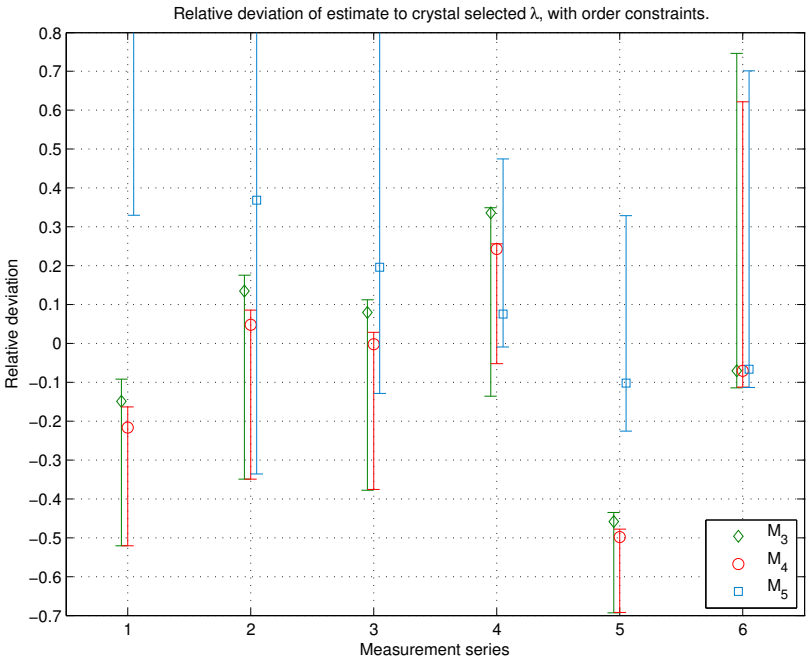

Figure 22: Relative deviation of λ estimates to crystal selected λ of each series. These estimates are formed according to the order constraints of (23).

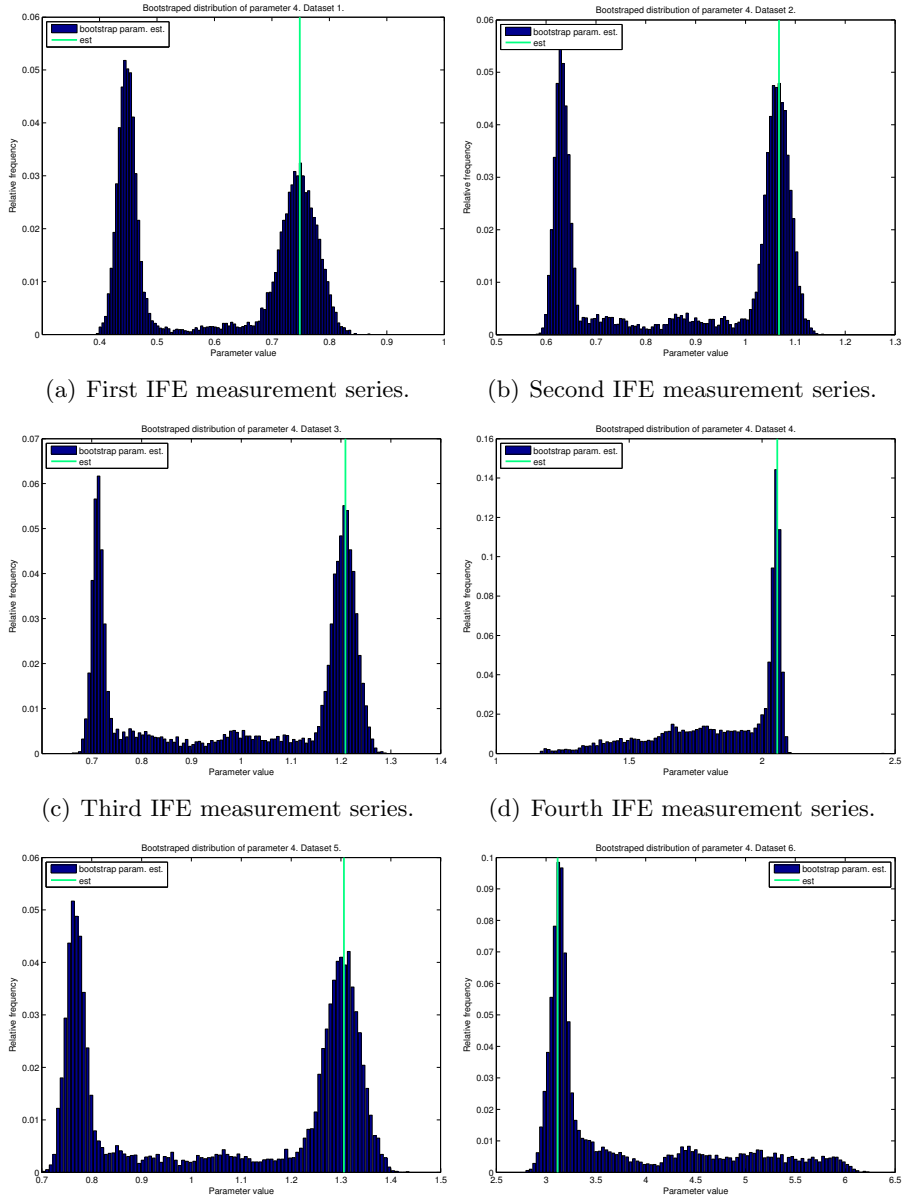

(a) First IFE measurement series.

(b) Second IFE measurement series.

(c) Third IFE measurement series.

(d) Fourth IFE measurement series.

(e) Fifth IFE measurement series.

(f) First HZB measurement series.

Figure 23: Distribution of λ estimates of M_3 for crystal data with the order constraints of (23).

Table 14: Parameter estimates of M_3 for the crystal data with the order constraints of (23).

$\hat{a}_1$	$\hat{a}_2$	$\hat{a}_3$	$\hat{a}_1 + \hat{a}_2 + \hat{a}_3$	$\hat{\lambda}$
425.155	425.155	425.155	1275.466	0.748
615.876	615.876	615.876	1847.628	1.067
725.009	725.009	725.009	2175.026	1.209
1384.685	1382.468	1382.468	4149.622	2.057
463.670	463.670	463.670	1391.009	1.306
44.123	-0.000	-0.000	44.123	3.115

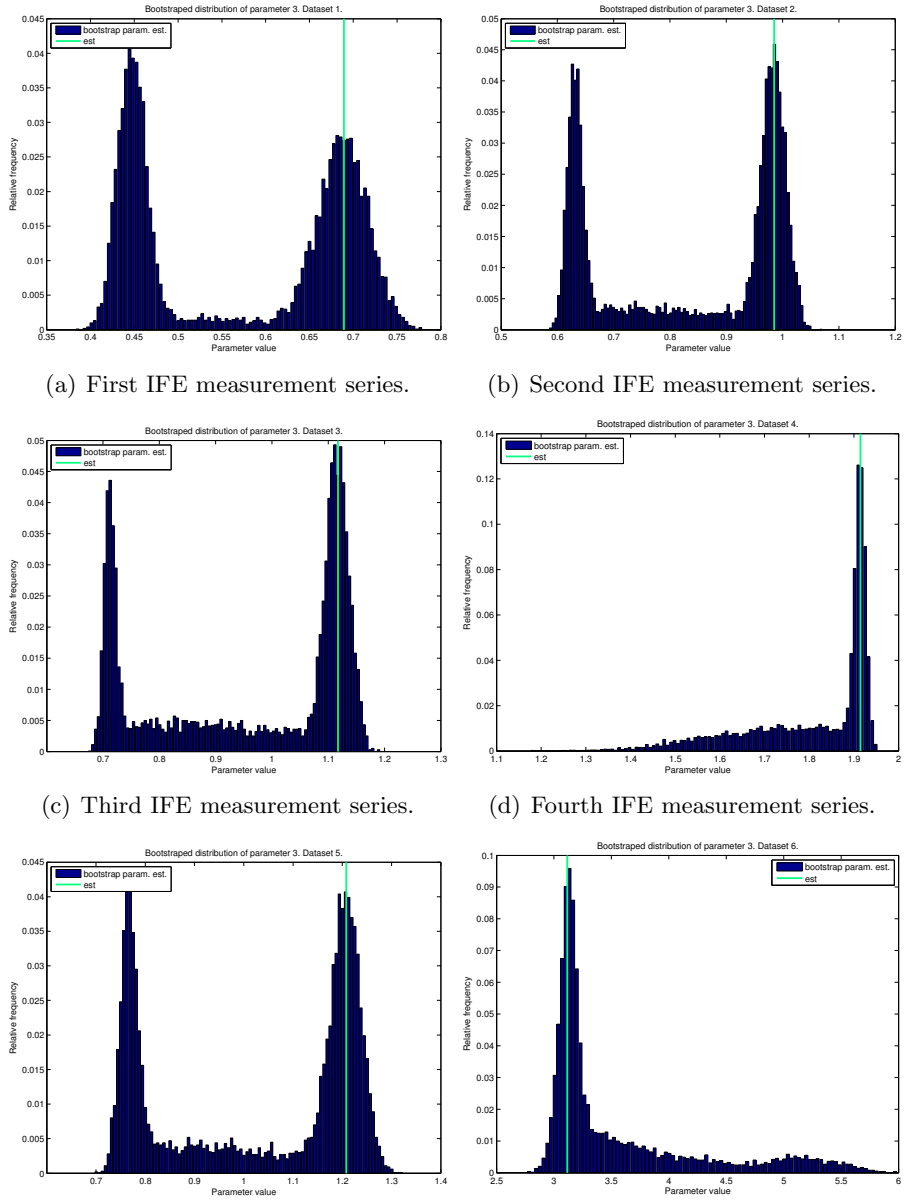

(a) First IFE measurement series.

(b) Second IFE measurement series.

(c) Third IFE measurement series.

(d) Fourth IFE measurement series.

(e) Fifth IFE measurement series.

(f) First HZB measurement series.

Figure 24: Distribution of λ estimates of M_4 for crystal data with the order constraints of (23).

Table 15: Parameter estimates of M_4 for the crystal data with the order constraints of (23).

$\hat{a}_1$	$\hat{a}_2$	$\hat{a}_1 + \hat{a}_2$	$\hat{\lambda}$
637.854	637.854	1275.708	0.689
924.129	924.129	1848.258	0.985
1088.007	1088.007	2176.013	1.117
2077.417	2077.417	4154.834	1.914
695.917	695.917	1391.835	1.208
44.123	0.000	44.123	3.115

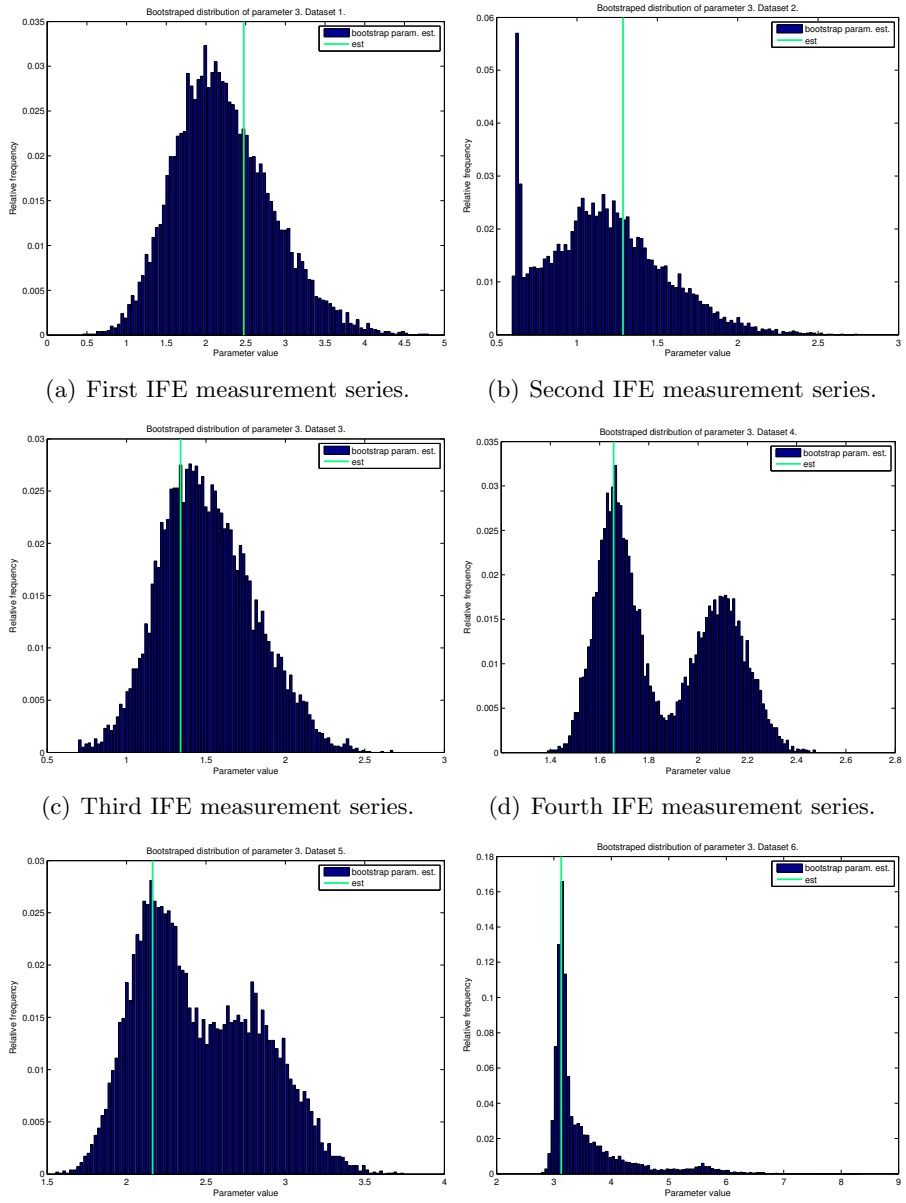

(a) First IFE measurement series. (b) Second IFE measurement series.

(c) Third IFE measurement series. (d) Fourth IFE measurement series.

(e) Fifth IFE measurement series. (f) First HZB measurement series.

Figure 25: Distribution of λ estimates of M_5 for crystal data with the order constraints of (23).

Table 16: Parameter estimates of M_5 for the crystal data with the order constraints of (23).

$\hat{a}_1$	$\hat{a}_2$	$\hat{b}$	$\hat{a}_1 + \hat{a}_2 + \hat{b}$	$\hat{\lambda}$
246.559	246.559	797.463	1290.582	2.477
748.833	748.833	355.349	1853.014	1.287
1333.982	0.000	853.154	2187.136	1.340
3276.261	0.000	887.228	4163.489	1.657
673.848	0.000	739.164	1413.012	2.165
44.025	0.000	0.104	44.129	3.127

5 Conclusions

The results of the estimation stage is evaluated in terms of how well the wavelength estimate resembles the expected wavelength, i.e. the wavelength reflected according to the crystal orientation.

General and specific limitations of the estimators, experimental setups and physical knowledge thereof are also addressed.

5.1 Simulated data

When constructing the simulated data no noise were added. Consequently a perfect fit to the data should be possible. The parameter estimates for the three first series succeed well in this aspect but the last fails, see Tables 5 and 6. This indicates that the minimisation problem is indeed multimodal and thus not convex. As a consequence the choice of initial point becomes more important. A better understanding of the minimisation problem itself is also needed. When a different set of initial values are applied the parameter estimates for M_6 on the last series of the simulated data converges differently. Another important factor would be to utilise physical constraints to the parameters when such assumptions could be made with high certainty. This would narrow down the search region and could thus give better estimates.

5.2 Single λ models

Looking at the results for the single wavelength model M_1, in Figure 11, its c estimates sits below the crystal set cross-section, indicating that a single wavelength model is not a good enough description of the data. The confidence bounds of M_2 however covers the expected value of c, for all but the first series of IFE, but are very wide. These wider confidence bounds are also seen for M_5 in Figures16 and 21. The conclusion drawn from this is that the addition of a background term does not contribute to the model but rather increaser the variance of the estimator.

5.3 Models for crystal data

Studying the bootstrapped distribution of M_3 - M_5, in Figures 18 - 20, with the natural parameter constraints of (20) some plots has multiple peaks, as if the λ estimates is a mix of unimodal distributions. This could indicate that the models cannot adequately capture the behaviour of the data and the possibility of additional λ contribution might need be investigated for these measurement series.

From Tables 11 - 13 it is clear that the estimates indicates a higher presence of $\lambda/3$ than λ itself. Furthermore, a $\lambda/2$ contamination is totally neglected by M_3, except for the HZB series. Though the latter is probably an artefact of the multi modality of the minimisation problem since the λ estimate is roughly twice that of M_4 which instead indicates a pure λ composition. The fact that the $\lambda/2$ term is neglected by the M_4 is interesting since both the second and last measurement series of the crystal data could have this contribution, according to Table 3.

5.4 Models for crystal data with order constraints

The bootstrapped distribution of M_3 - M_5, estimated with the order constraints of (23), in Figures 23 - 25 also displays the behaviour of a mixed distribution though somewhat less present for M_5. Looking at the point estimates of Tables 14 - 16 the a_j estimates are generally found at the border. Since the estimates converges to a point at the border of the parameter space this could indicate that an assumption of falling wavelength proportions does not hold. Though the confidence intervals of these estimates are narrower than for the estimates with only natural constraints on the parameters. Statistical tests could be used to test if the order restriction can be rejected, cf. [17]. However, the HZB estimates all indicate a pure λ beamline thus the question whether the order restrictions is valid or not is mainly of interest for the IFE data. This could also be taken as an indication of problems with the IFE beamline itself.

The order constraint has its origin in the current understanding of the crystal monochromators applied, as well as properties of the experiment setup itself. Investigating these properties further would be beneficial in both evaluation and construction of models and constraints.

5.5 General comments for all models

In Figures 16 and 21 it can be seen that both M_3 and M_4 performs well and its confidence bounds cover the expected wavelength for most series. However the a_j estimates for $\lambda/3$ are larger than those of λ indicating a beam clearly dominated by the higher order contaminations. This is not in line with the current understanding of the properties of the crystal used. It is unclear whether this contradicting results is due to convergence to a local minimum or if the properties the setup in fact support these results. For the estimations with order constraints on the a_j parameters the estimates converges to a point at the border of the parameter space. This also indicates that an order restriction could be invalid, though this could be statistically tested.

Perhaps a predefined search region for the λ estimates governed by the orientation of the crystal monochromator could be used in order to constrain the wavelength estimates. A more thorough analysis of how the choice of initial point in the minimisation algorithm effects the results could be carried out to possibly improve the performance of the minimisation step.

5.6 Limiting factors and possible improvements

A general limitation for the estimation problem is the small number of data points in the measurement series. Therefore asymptotic properties of the estimator cannot be assured to hold. Longer measurement series, i.e. more data points, would increase the accuracy of the estimator. However the number of data points in the series are similar to the number of detection cells, in the detector design being developed at ESS. It is methods for characterising beams with this design that is desired, thus it might be wise to develop such methods under the conditions it will operate and therefore the addition of more data points is unwanted.

Another important assumption is that the intensity of the beam is constant during the time a complete measurement series is obtained and that its wavelength distribution is constant. A low efficiency detector, similar to that of the HZB setup, could be used as beam monitor, before the crystal, to ensure that the first assumption is fulfilled as a measurement series is obtained. This is a technique already used at other facilities.

Better knowledge of the detectors used in the experiment setups is required to be able to eliminate the possibility that the detector saturates. This means that some neutrons will create a pulse in the detector that will not be detected. This effect will have a greater impact as the incident rate of neutrons is higher, e.g. for points with few blades in the beam, or for wavelengths where the detector efficiency is higher. The possible impact of this effect is unknown for the current data but could be a possible source of systematical error for some early points of the measurement series with higher rates.

A well characterised detector could also make it possible to estimate wavelength proportions p_j. This would allow for more accurate constraints on the exponential coefficients, when backed up by the physics of the experimental line-up.

For the IFE data a possible source of error where discovered. The crystal monochromator was not properly fixed as the measurements where obtained. Instead it had some possibility to move which would change its angle relative the incident beam and thus also the expected wavelength reflected from the crystal. It is unclear how big this impact could be in the measurements, if any.

A summary of the above suggested improvements is made below.

(i) Analyse of the intensity profile of the IFE beamline, and possibly the crystal properties, to verify that the assumption of falling wavelength proportions is valid.

(ii) Include a low efficiency detector as beam monitor at the IFE setup.

(iii) Eliminate or control possibility of saturation in the detector.

(iv) Find a satisfying parametrisation of detector efficiency in order obtain estimates of p_j and the possibility of applying more accurate parameter constraints where this is supported by physics.

(v) Obtain new measurements as the above improvements has been made.

In general the analysis of the results are made in the light of the current physical understanding of the experimental line-up. To some extent this is based on assumptions that has not been verified for the specific setup. A better understanding of the physics of the individual experimental setups would be of great help when it comes to whether it is the model, estimator or the physical assumptions of the setup that should be questioned but also help in the general evaluation and constructions of models for the given data.

Even if a lot of work remains to be done, this approach has already proven to be useful as it has helped in the work to assure the quality of

the IFE beamline. When a more accurate understanding of the physical properties of the experimental line-up is achieved these cloud be used to impose more precise restrictions of the parameters. Together with deeper mathematical understanding of the optimisation process this would really help achieving satisfying techniques for neutron beam modelling.

6 References

[1] S. Peggs et al. Technical design report, ess-2013-001. Technical report, European Spallation Source AB, 2013.

[2] A. Cho. Helium-3 shortage could put freeze on low-temperature research. *Science*, page 778, 2009.

[3] Zhehui Wang and C.L. Morris. Multi-layer boron thin-film detectors for neutrons. *Nuclear Instruments and Methods in Physics Research A*, page 323, 2011.

[4] Dragi Anevski and Richard Hall-Wilton. Statistical methods for energy determination in neutron detector systems. Technical report, Mathematical Sciences Lund University and ESS, 2012.

[5] J. Birch I. Defendi R. Hall-Wilton C. Höglund L. Hultman D. Seiler K. Zeitelhack I. Stefanescu, Y. Abdullahi. Development of a novel macrostructured cathode for large-area neutron detectors based on the 10b-containing solid converter. *Nuclear Instruments and Methods In Physics Research A*, 727:109–125, 2013.

[6] J. Birch I. Defendi R. Hall-Wilton C. Höglund L. Hultman M. Zee K. Zeitelhack I. Stefanescu, Y. Abdullahi. A 10b-based neuron detector with stacked multiwire proportional counters and macrostructured cathodes. *JINST*, 8:P12003, 2013.

[7] A. Khaplanov et al. Investigation of gamma-ray sensitivity of neutron detectors based on thin converter films. *JINST*, 8:P10025, 2013.

[8] Roger Pynn. Neutron scattering - a primer, 1990.

[9] B. T. M. Willis and C. J. Carlile. *Experimental Neutron Scattering*, pages 22–26. Oxford University Press, 2009.

[10] G. Rhodes. *Crystallography made crystal clear*. Academic Press, second edition, 1999.

[11] B. T. M. Willis and C. J. Carlile. *Experimental Neutron Scattering*, pages 89–90. Oxford University Press, 2009.

[12] Brookhaven National Laboratory. http://www.nndc.bnl.gov/sigma/index.jsp?as=10&lib=endfb7.1&nsub=10.

[13] T. Rockafellar. *Convex Analysis*. Princeton University Press, 1970.

[14] R.I. Jennrich. Asymptotic properties of non-linear least squares estimators. *The Annals of Mathematical Statistics*, 40:633–643, 1969.

[15] A.W. van der Vaart. *Asymptotic Statistics*. Cambridge University Press, 1998.

[16] John Fox. *Applied Regression Analysis and Generalized Linear Models*. Sage, second edition, 2008.

[17] F.T. Wright Tim Robertson and R.L Dykstra. *Oder Restricted Statistical Inference*. John Wiley & Sons, 1988.